Geobiology

WILEY

gebiology

ORIGINAL ARTICLE OPEN ACCESS

Living in Their Heyday: Iron-Oxidizing Bacteria Bloomed in Shallow-Marine, Subtidal Environments at ca. 1.88 Ga

Alex Kovalick[1] | Andy W. Heard[2,3] | Aleisha C. Johnson[3,4] | Clara S. Chan[5] | Luke Ootes[6] | Sune G. Nielsen[2,7] | Nicolas Dauphas[3] | Bodo Weber[8] | Andrey Bekker[1]

[1]Department of Earth and Planetary Sciences, University of California, Riverside, California, USA | [2]Department of Geology & Geophysics, Woods Hole Oceanographic Institution, Woods Hole, Massachusetts, USA | [3]Origins Laboratory, Department of the Geophysical Sciences, The University of Chicago, Chicago, Illinois, USA | [4]Department of Geosciences, University of Arizona, Tucson, Arizona, USA | [5]Department of Earth Sciences, University of Delaware, Newark, Delaware, USA | [6]British Columbia Geological Survey, Ministry of Energy, Mines and Low Carbon Innovation, Victoria, British Columbia, Canada | [7]CRPG, CNRS, Université de Lorraine, Nancy, France | [8]Departamento de Geología, Centro de Investigación Científica y de Educación Superior de Ensenada, CICESE, Ensenada, Baja California, Mexico

Correspondence: Alex Kovalick (fkova001@ucr.edu)

Received: 4 March 2024 | **Revised:** 1 October 2024 | **Accepted:** 3 November 2024

Funding: This work was supported by WHOI Postdoctoral Scholarship, The Petroleum Foundation of the American Chemical Society (624840ND2), Society of Economic Geologists—Graduate Student Fellowship Program, Polar Continental Shelf Program, NASA Exobiology (80NSSC22K1628), CONTACTyT infrastructure (INFR-2016-01-269082), NSERC Discovery and Accelerator Grants, and National Science Foundation Earth Sciences Postdoctoral Fellowships (1952809).

Keywords: granular iron formations | iron isotope ratios | iron-oxidizing bacteria | Paleoproterozoic pO_2 | rare earth elements

ABSTRACT

The majority of large iron formations (IFs) were deposited leading up to Earth's great oxidation episode (GOE). Following the GOE, IF deposition decreased for almost 500 Myr. Subsequently, around 1.88 Ga, there was widespread deposition of shallow-water granular iron formations (GIF) within a geologically short time interval, which has been linked to enhanced iron (Fe) supply to seawater from submarine hydrothermal venting associated with the emplacement of large igneous provinces. Previous studies of Fe-rich, microfossil-bearing stromatolites from the ca. 1.88 Ga Gunflint Formation on the Superior craton suggested direct microbial oxidation of seawater $Fe^{2+}_{(aq)}$ by microaerophilic, Fe-oxidizing bacteria (FeOB), as a driver of GIF deposition. Although Fe-rich, microfossil-bearing stromatolites are common in 1.88 Ga GIF deposits on several cratons, combined paleontological and geochemical studies have been applied only to the Gunflint Formation. Here, we present new paleontological and geochemical observations for the ca. 1.89 Ga Gibraltar Formation GIFs from the East Arm of the Great Slave Lake, Northwest Territories, Canada. Fossil morphology, Rare Earth element (REE) concentrations, and Fe isotopic compositions support Fe oxidation by FeOB at a redoxcline poised above the fair-weather wave base. Small positive Eu anomalies and positive ε_{Nd} (1.89 Ga) values suggest upwelling of deep, Fe-rich, hydrothermally influenced seawater. While high $[Fe^{2+}_{(aq)}]$ combined with low atmospheric pO_2 in the late Paleoproterozoic would have provided optimal conditions in shallow oceans for FeOB to precipitate Fe oxyhydroxide, these redox conditions were likely toxic to cyanobacteria. As long as local O_2 production by cyanobacteria was strongly diminished, FeOB would have had to rely on an atmospheric O_2 supply by diffusion to shallow seawater to oxidize $Fe^{2+}_{(aq)}$. Using a 1-D reaction dispersion model, we calculate $[O_{2(aq)}]$ sufficient to deplete an upwelling $Fe^{2+}_{(aq)}$ source. Our results for GIF deposition are consistent with late Paleoproterozoic pO_2 estimates of ~1%–10% PAL and constraints for metabolic $[O_{2(aq)}]$ requirements for modern FeOB. Widespread GIF deposition at ca. 1.88 Ga appears to mark a temporally restricted episode of optimal biogeochemical conditions in Earth's history when increased hydrothermal $Fe^{2+}_{(aq)}$ sourced from the deep oceans, in combination with low mid-Paleoproterozoic atmospheric pO_2, globally satisfied FeOB metabolic $Fe^{2+}_{(aq)}$ and $O_{2(aq)}$ requirements in shallow-marine subtidal environments above the fair-weather wave base.

1 | Introduction

Precambrian-banded iron formations (BIFs) and granular iron formations (GIFs), collectively referred to as iron formations (IFs), are iron (Fe)-rich (bearing at least 15 wt.% Fe) sedimentary rocks that were deposited episodically throughout Earth's history (Bekker et al. 2014). Temporally, massive IF deposition has been influenced by both the evolution of atmospheric pO_2 and the submarine emplacement of large igneous provinces (LIPs; Bekker et al. 2014). The development of Earth's O_2-rich atmosphere occurred in two major steps (Lyons, Reinhard, and Planavsky 2014): the Great Oxidation Episode (GOE) (Holland 2002; Bekker et al. 2004; Gumsley et al. 2017) that occurred between ca. 2.43 and 2.06 Ga and the Neoproterozoic Oxygenation Event (NOE) (Och and Shields-Zhou 2012) that took place between 0.80 and 0.55 Ga. A variety of environmental controls that are not mutually exclusive likely contributed to the deposition of massive IFs. Archean and Paleoproterozoic IFs are temporally associated with LIPs, dike swarms, and volcanogenic massive sulfide deposits, revealing a link between IF deposition and increased iron flux to the oceans driven by hydrothermal alteration of oceanic crust (Isley and Abbott 1999; Bekker and Holland 2012; Bennett et al. 2014). Supercontinent assembly has also been inferred as a contributing factor for massive IF deposition (Barley, Bekker, and Krapež 2005; Bekker et al. 2014). Iron formation deposition leading up to the NOE coincides with Snowball Earth glaciations and likely reflects a buildup of $Fe^{2+}_{(aq)}$ in the oceans under Sturtian and Marinoan ice sheets (Hoffman et al. 2017; Lechte et al. 2018, 2019). The relative influence of these environmental controls on IF deposition at other times in Earth's history remains underexplored and associated biogeochemical processes may also have played a key role. Most major IFs were deposited between 2.7 and 2.45 Ga, leading up to the GOE. Iron formation deposition was limited for more than 500 Myr following the start of the GOE until ca. 1.88 Ga when shallow-marine GIFs were deposited on multiple, paleogeographically disconnected cratons (Pesonen et al. 2021; Buchan et al. 2016; Bekker et al. 2014). Several GIFs in the Lake Superior region and Labrador Trough of the Superior craton, and the Frere Formation GIFs in the Earaheedy basin of the Yilgarn craton, Western Australia have been dated to ca. 1.88 Ga (Fralick, Davis, and Kissin 2002; Schneider et al. 2002; Rasmussen et al. 2012). So far, each has been shown to record remarkably similar geochemical information and preserve filamentous and spherical microfossils in Fe- and Si-rich stromatolitic facies (Barghoorn and Tyler 1965; Cloud 1965; Knoll and Simonson 1981; Walter, Goode, and Hall 1976). Similar trace element and REE+Y compositions consistent with Fe and Mn cycling across a redoxcline have also been reported for some of these GIFs (Planavsky et al. 2010). Although smaller-scale GIFs were episodically deposited throughout the Archean and Proterozoic with the earliest example documented at ca. 2.95 Ga (Smith et al. 2017), the conspicuous deposition of voluminous GIFs on several paleogeographically distinct cratons within a relatively short time interval at ca. 1.88 Ga is reminiscent of massive IF deposition leading up to the GOE, prompting investigation into potentially shared driving mechanisms.

The widespread deposition of oolitic GIFs at this time in shallow-water settings at and above the fair-weather wave base (FWWB) requires the development of Fe-rich conditions in the deep oceans under the post-GOE oxygenated atmosphere, necessitating redox-stratified conditions in multiple sedimentary basins. Redox-sensitive Rare Earth elements and Yttrium (REE+Y) have been used in studies of redox-stratified basins in general, and those where ca. 1.88 Ga GIFs were deposited, to constrain the depositional setting with respect to the redoxcline. Preferential scavenging of cerium (Ce) and light REEs (LREEs) onto reactive Fe and manganese (Mn) oxyhydroxides, clay minerals, and organic matter particle surfaces at and above the redoxcline, and preferential retention of yttrium (Y) in seawater dictates the relative abundance of redox-sensitive REE+Y in the water column, resulting in variable Ce anomalies, light to heavy REE (LREE/HREE) ratios, and Y/Ho (Bau 1999; Bau and Dulski 1996; Bau, Möller, and Dulski 1997; Nozaki, Zhang, and Amakawa 1997). The fractionation recorded by each of these proxies is therefore only partially and indirectly dependent on Fe and Mn oxyhydroxide cycling. While the relative degree to which each of these proxies is specifically redox-sensitive remains a topic of active study, in IF-forming environments where little organic matter and detrital material are buried, Fe and Mn oxyhydroxides have been considered dominantly responsible for shaping REE+Y patterns (Bau and Dulski 1996; Planavsky et al. 2010). Enhanced scavenging onto Fe and Mn oxyhydroxide minerals in these redox-stratified environments therefore develops relative depletion of Ce and LREE, and enrichment of Y in shallow waters above the redoxcline, whereas subsequent reduction of these oxyhydroxides at or below the redoxcline enriches deeper waters in these elements (Sholkovitz and Elderfield 1988; German, Holliday, and Elderfield 1991; Sholkovitz, Shaw, and Schneider 1992; Byrne and Sholkovitz 1996; Bau, Möller, and Dulski 1997; Nozaki, Zhang, and Amakawa 1997). Manganese-oxyhydroxide precipitation, which requires free O_2 and higher Eh conditions than those for Fe oxyhydroxide precipitation (Canfield and Thamdrup 2009), largely controls the Ce budget in oxygenated waters by mediating oxidation of adsorbed Ce^{3+} to Ce^{4+} (Moffett 1994; Bau 1999; Tebo et al. 2005; Bau and Koschinsky 2009). Seawater in redox-stratified basins may in turn develop dissolved REE+Y profiles with positive Ce anomalies, LREE/HREE > 1, and super-chondritic Y/Ho ratios above the redoxcline and the opposite below it. These signals can be captured by Fe oxyhydroxide precipitates above and below the redoxcline and studies of REE+Y in ca. 1.88 Ga GIFs have demonstrated the presence of shallow redoxclines in these basins (Planavsky et al. 2010 and references therein).

One likely culprit for driving ca. 1.88 Ga GIF deposition might be an overwhelming source of $Fe^{2+}_{(aq)}$ to the oceans. Condie, Des Marais, and Abbott (2000) recognized a high rate of continental crust production at ca. 1.9 Ga and suggested that this was caused by enhanced emplacement of oceanic LIPs associated with a series of widespread mantle plume events during a geologically short time interval. Rasmussen et al. (2012) further linked GIF deposition to elevated hydrothermal activity related to LIP-associated submarine volcanism. They argued that resulting hydrothermal fluid circulation through oceanic crust leached an excess of Fe^{2+} from mafic volcanics and released it to the deep ocean. These reduced hydrothermal fluids would have overwhelmed the oceans with $Fe^{2+}_{(aq)}$ and other reduced species, shoaling the redoxcline and separating deep ferruginous from surface oxic waters in shallow-marine settings above the FWWB (Rasmussen et al. 2012). Sindol et al. (2022) recently

found that the positive Europium (Eu) anomaly, a proxy for high-temperature hydrothermal fluid input, is similar in both deep- and shallow-water settings recorded by the ca. 1.88 Ga Sokoman Formation (Findlay et al. 1995). These findings may be consistent with the whole ocean being dominated by submarine, LIP-induced, hydrothermal activity.

Alternatively, early studies considered enhanced continental weathering as a possible source of Fe for GIF deposition. An inferred mafic continental crust composition in the Archean (Condie 1993), a topic of significant debate recently (see Greber et al. 2017 for an alternative view), would have increased the delivery of organically chelated Fe with riverine systems (James 1954; Lepp and Goldich 1964). Based on the calculated Fe flux of about 2×10^{13} g/year required to deposit the BIFs of the Hamersley Province in Western Australia, exceeding that of the largest modern rivers by several orders of magnitude, Holland (1973) concluded that reasonable riverine Fe flux from the continents would not be sufficient to support deposition of the Hamersley Province BIFs. Recent calculations for riverine Fe flux to ancient oceans, based on Fe/Mn ratios and an assumption that Fe export from rivers scales with CO_2 degassing over time, still fall short by orders of magnitude, estimating that of the Proterozoic to be around 1.8×10^{11} g/year (Dauphas et al. 2025). Recent studies have not abandoned the idea of a terrestrial Fe source by invoking a mix of both hydrothermal and continental (via microbial Fe^{3+} reduction in sediments) sources of $Fe^{2+}_{(aq)}$ to fuel IF deposition (Li, Beard, and Johnson 2015; Wang et al. 2024). With the continued application of novel geochemical techniques (Haugaard et al. 2016; Konhauser et al. 2017), the dominant Fe source to the Precambrian oceans, whether submarine hydrothermal activity or continental weathering, remains a subject of debate.

While an increased supply of submarine, hydrothermal $Fe^{2+}_{(aq)}$ to shallow-marine settings appears to have been a likely factor in ca. 1.88 Ga GIF deposition (Rasmussen et al. 2012), contributing to microfossil preservation upon Fe and Si mineralization, late Paleoproterozoic pO_2 may also have played an important role. Although the exact level is still debated (Frei et al. 2009; Babechuk, Kleinhanns, and Schoenberg 2017; Toma et al. 2019; Zhang et al. 2016; Bellefroid et al. 2018; Large et al. 2019; Steadman et al. 2020), it is widely accepted that late Paleoproterozoic pO_2 was overall higher than that before the GOE, but lower than that of the Phanerozoic (Lyons, Reinhard, and Planavsky 2014; Lyons et al. 2021). Eyster et al. (2021) recently suggested that ca. 1.88 Ga GIFs of the Gogebic Range in the Lake Superior area are not stratigraphically associated with volcanic rocks and, therefore, a decrease in atmospheric oxygen rather than an increase in submarine, hydrothermal flux of reductants might be responsible for a shallower redoxcline leading to GIF deposition. It thus seems likely that low atmospheric pO_2 in the late Paleoproterozoic also contributed to priming these settings for GIF deposition around 1.88 Ga.

Irrespective of whether the source of $Fe^{2+}_{(aq)}$ or background atmospheric pO_2 drove global scale, ca. 1.88 Ga GIF deposition, the development of widespread, ferruginous (anoxic and Fe^{2+}-rich) conditions around 1.88 Ga coincided with the widespread preservation of microbial ecosystems in stromatolitic facies, broadly named the Gunflint biota (Barghoorn and Tyler 1965; Cloud 1965). This microfossil assemblage provides unique insight into the ecosystems that thrived in these ferruginous seawater settings and may have played a key role in GIF deposition. Based on paleoenvironmental context, it has been argued that this microfossil assemblage is a remnant of organisms that directly or indirectly oxidized seawater $Fe^{2+}_{(aq)}$, resulting in Fe^{3+} oxyhydroxide precipitation (Barghoorn and Tyler 1965; Cloud 1965). Twisted and coiled, filamentous morphologies found in some specimens were compared to those of the modern cyanobacteria *Spirulina* and chemolithotrophic, microaerophilic, Fe oxidizing bacteria (FeOB), Zetaproteobacteria *Mariprofundus ferrooxydans*; both alternatives were initially considered by Barghoorn and Tyler (1965). Despite extensive following studies, the unresolved affinity of these fossils remains a central point of discussion, as it might provide key insight into the role of indirect biological oxidation by cyanobacterial O_2 production or direct biological Fe oxidation by FeOB in depositing GIFs.

Iron isotope values (δ^{56}Fe; reported as the per mil deviation of $^{56}Fe/^{54}Fe$ in the sample relative to the IRMM-014 standard) can be used as a tracer of Fe oxidation in the sedimentary record (see Johnson, Beard, and Weyer 2020 for a recent review). Laboratory experiments have quantified Fe isotope fractionation factors for the major Fe oxidation pathways proposed for IF deposition. Both abiotic and biologically mediated $Fe^{2+}_{(aq)}$ oxidation and Fe oxyhydroxide precipitation preferentially select heavier Fe isotopes in the instantaneous oxyhydroxide product. The effect of this fractionation on the δ^{56}Fe values of $Fe^{2+}_{(aq)}$ in the fluid and of the resulting Fe oxyhydroxide precipitates is rate dependent (see Johnson, Beard, and Weyer 2020 and references therein) and the array of studied processes capable of producing Fe oxyhydroxides with high δ^{56}Fe values from oxidation of $Fe^{2+}_{(aq)}$ is extensive, including spontaneous abiotic ferrihydrite precipitation (Bullen et al. 2001), abiotic, UV light-induced photo-oxidation (Nie, Dauphas, and Greenwood 2017), and a variety of microbial oxidation mechanisms (Mulholland et al. 2015; Croal et al. 2004; Swanner, Wu et al. 2015; Kappler et al. 2010; Johnson, Beard, and Weyer 2020). Typically, Fe isotope fractionation factors quantified by these studies lie in the range of ~1.0‰–1.5‰, which are expressed as the difference between the δ^{56}Fe of the $Fe^{2+}_{(aq)}$ in the residual fluid and the resulting precipitate. In contrast, oxygen production by cyanobacteria can generate sufficiently high O_2 in local microenvironments to quantitatively oxidize $Fe^{2+}_{(aq)}$, as was observed in modern cyanobacterial mats by Trouwborst et al. (2007). This quantitative oxidation would preclude the expression of Fe isotope fractionation, resulting in uniform values in the precipitate, which reflect that of the source fluids.

Circa 1.88 Ga GIFs are a unique target for Fe isotopic study because they host Fe-rich stromatolites that contain microfossils that might be remnants of the organisms responsible for Fe oxidation. Combined paleontological and geochemical study of the ca. 1.88 Ga Animikie basin stromatolitic GIFs argued for a prevalence of FeOB among the Gunflint biota (Planavsky et al. 2009). A wide range of δ^{56}Fe values in GIF units with fossil-bearing stromatolites, having more positive δ^{56}Fe values than those lacking fossils, aligns with a varying extent of partial, direct Fe oxidation by FeOB rather than quantitative, indirect oxidation in well-oxygenated environments via O_2 produced by cyanobacteria. In contrast to those late Paleoproterozoic examples,

δ^{56}Fe values for individual lamina in Fe-rich stromatolites from the 2.46–2.43 Ga Griquatown Iron Formation GIF from the Kaapvaal craton in South Africa overlap with bulk-rock δ^{56}Fe values within a small range (Heard et al. 2022). These findings were argued to be consistent with quantitative, indirect, biological oxidation at the depositional site via cyanobacterial oxygen production just prior to the GOE, in agreement with Mn and Ce concentration data (Heard et al. 2022).

Considering these recent findings, the Fe isotope composition of Fe-rich stromatolites has proven to be a useful tool for investigating Fe oxidation mechanisms, revealing ecological information otherwise unattainable by paleontological data alone. The widespread proliferation of microaerophilic, Fe oxidizing ecosystems in shallow-marine, subtidal environments, above the FWWB, would constitute a unique event in Earth's history when $[Fe^{2+}_{(aq)}]$ and $[O_{2(aq)}]$ in shallow, coastal settings were both within the optimal ranges for FeOB to bloom. However, geochemical data supporting this hypothesis remain restricted to the Animikie basin GIFs (Planavsky et al. 2009). We present herein a combined paleontological and geochemical study of GIFs and Fe-rich stromatolites from the ca. 1.89 Ga Gibraltar Formation, southern Slave craton (a landmass disconnected from the Superior craton at the time of deposition), Northwest Territories, Canada (Figure 1) to further evaluate the degree to which microaerophilic, Fe-oxidizing ecosystems were globally widespread at around 1.88 Ga. Based on the results, we consider the broader implications of the development of such biogeochemical conditions for FeOB and the proliferation of these Fe-oxidizing ecosystems in GIF-forming environments with respect to global atmospheric and ocean redox conditions, adding a microbial metabolism perspective to efforts aimed at constraining the redox structure of Earth's late Paleoproterozoic marine environments during deposition of the ca. 1.88 Ga GIFs.

2 | Geologic Setting

The Paleoproterozoic East Arm basin contains a succession of sedimentary and lesser volcanic rocks, preserved within and

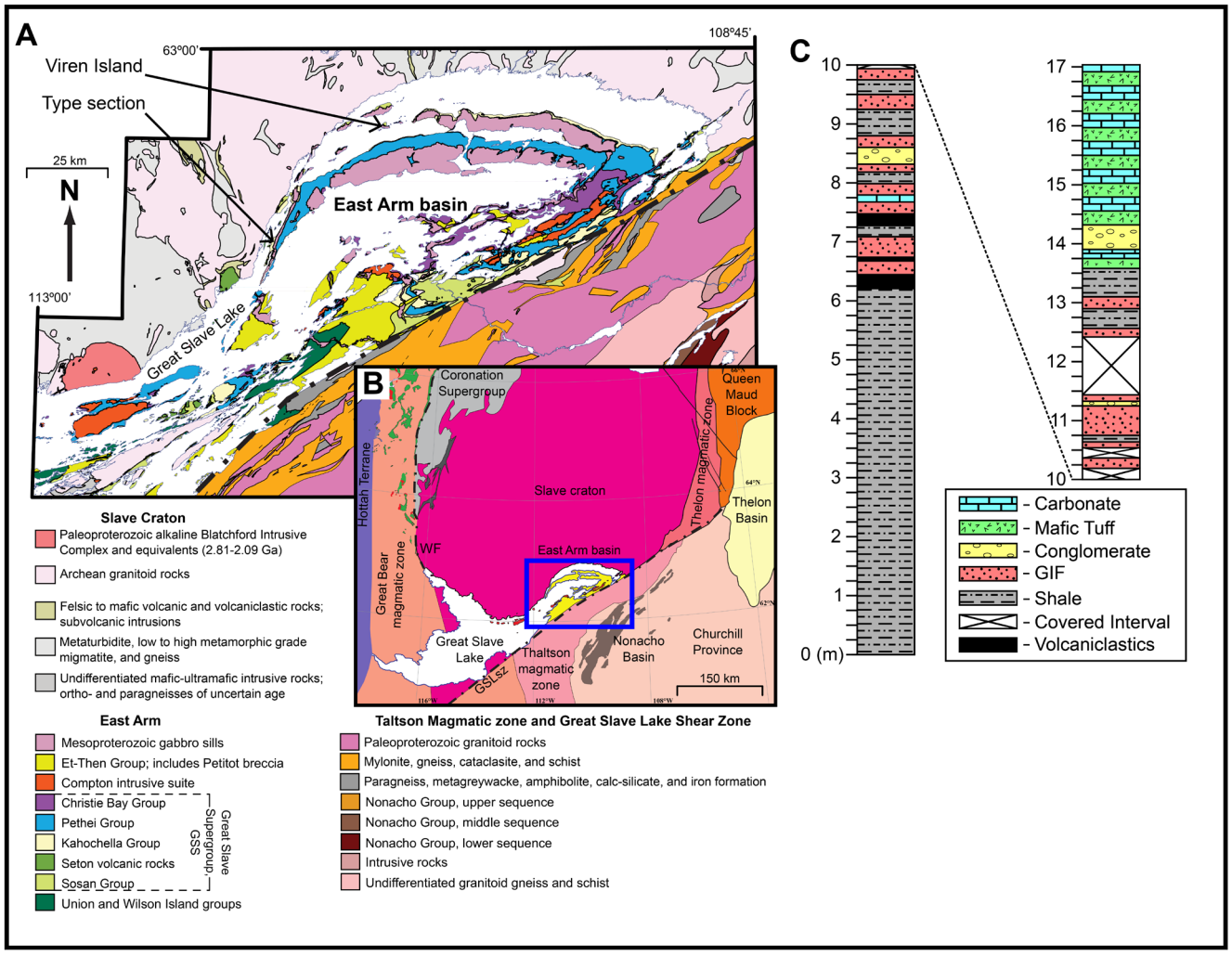

FIGURE 1 | Map and stratigraphy of the Paleoproterozoic East Arm basin. (A) Geologic map of the East Arm of the Great Slave Lake (adapted from Van Breemen et al. 2013) showing the location of the type and Viren Island sections with black arrows. (B) The inset map shows the present-day position of tectonic units in northwest Canada (adapted from Van Breemen et al. 2013); GSLsz, Great Slave Lake shear zone; WF, Wopmay Fault. The area within the blue box is the approximate location of the East Arm of the Great Slave Lake where studied material was collected. (C) Stratigraphic column of the Type section of the Gibraltar Formation.

around the East Arm of Great Slave Lake, Northwest Territories, Canada. A generalized north to south stratigraphic section of the East Arm basin (modified from Hoffman, Dewey, and Burke 1974) is presented in Figure 2. The basin developed on the southern margin of the Archean Slave craton and is bounded to the south by the ca. 1.95 Ga Great Slave Lake shear zone (GSLsz; Berman et al. 2023) and younger brittle faults (Figure 1). The stratigraphic overview presented here generally follows Hoffman (1988a). The Union Island Group (ca. 2.05 Ga; Sheen et al. 2019) was deposited unconformably on the Archean basement and is the oldest stratigraphic unit in the East Arm basin. Sheen et al. (2019) demonstrated OIB- and E-MORB-like geochemical signatures for two basalt packages of the Union Island Group, supporting rifting early in the development of the basin, but the subsequent basinal evolutionary history remains poorly constrained. The marginal-marine ca. 1.93 Ga Wilson Island Group (Bowring, Schmus, and Hoffman 1984; Johnson 1990) might have been deposited during extension related to orogen collapse, following the collision of the Slave and Rae cratons at ca. 1.95–1.94 Ga (Berman et al. 2023). The Union Island and Wilson Island groups are nowhere in stratigraphic contact but are both overlain by the <1.9 Ga Great Slave Supergroup (GSS), a thick (up to 12 km in thickness), generally unmetamorphosed, sedimentary succession exposed across the NE-trending East Arm synclinorium and cropping out on islands and mainland shores of Great Slave Lake (Figure 1; Hoffman 1968; Pope and Grotzinger 2003). The GSS includes the Sosan, Kahochella, Pethei, and Christie Bay groups and is unconformably overlain by the Et-Then Group. The minimum depositional age for the supergroup is 1866.9 ± 0.9 Ma, based on the CA-ID-TIMS U–Pb zircon date for the Compton Intrusive suite monzodiorite (Hoffman et al. 2023).

It was originally suggested that the East Arm basin developed as a failed rift (Hoffman 1973). An alternative model attributes GSS basin development to syn-collisional transtension during an oblique collision between the Slave and Rae cratons along the NE-trending GSLsz (Bowring, Schmus, and Hoffman 1984; Hoffman 1987, 1988b). The Sosan, Kahochella, and Pethei groups of the GSS were deposited after the Slave-Rae collision to the east and synchronously, but distally to syn-collisional,

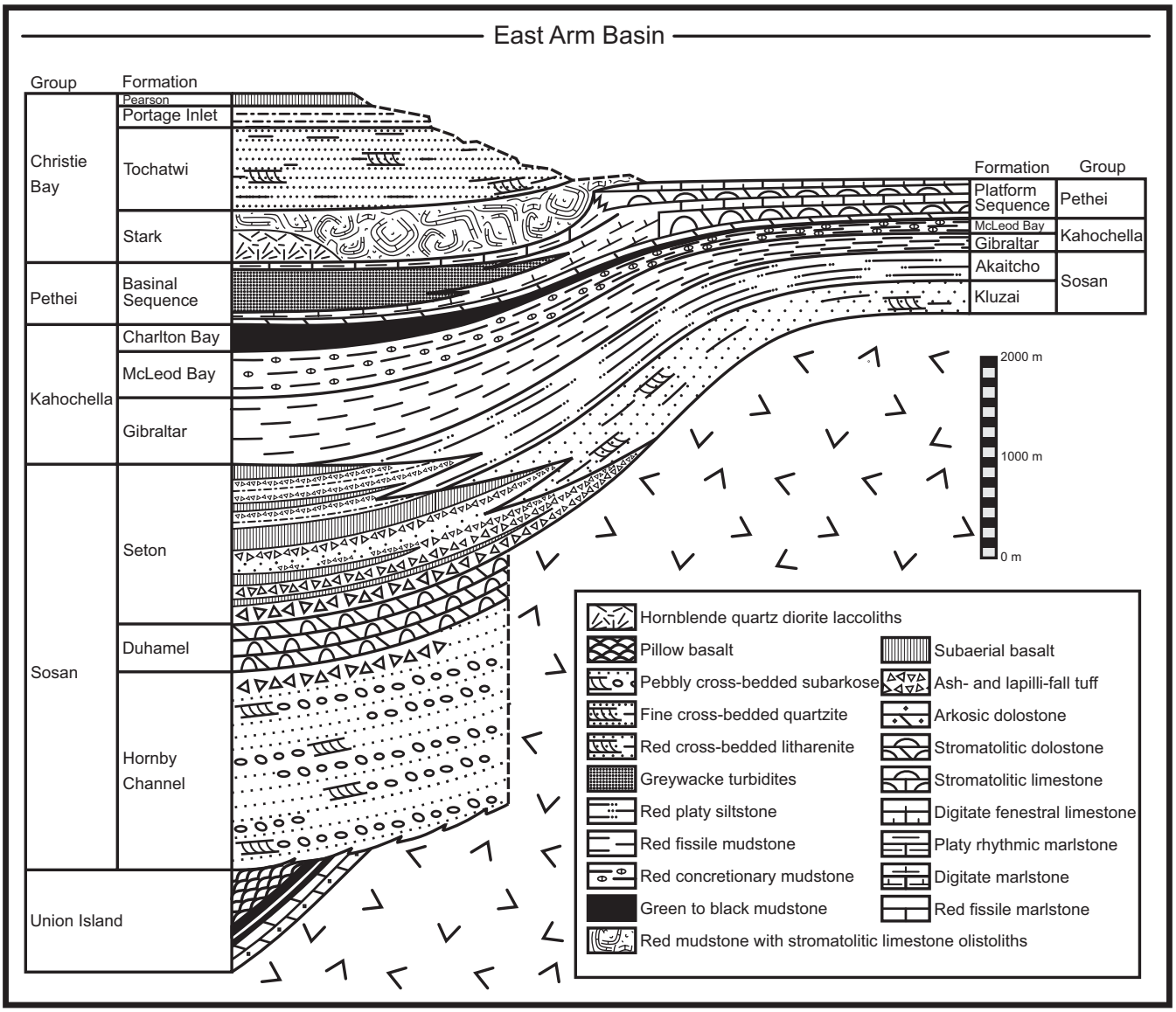

FIGURE 2 | A generalized N-S cross section for the East Arm basin and laterally equivalent platform sedimentary units (modified from Hoffman, Dewey, and Burke 1974).

tectono-magmatic activity in the Wopmay orogen to the west of the Slave craton (Hildebrand, Hoffman, and Bowring 2010; Jackson et al. 2013; Ootes et al. 2015, 2016). The lower Sosan Group contains the fluvio-deltaic Kluzai Formation and the overlying Akaitcho River Formation, deposited early in the renewed basin development with paleocurrents indicating flow to the southwest (Hoffman 1968). Stratigraphically above, there are red and green shales with interbedded GIF of the Gibraltar Formation in the lower Kahochella Group that were interpreted to be shallow-marine deposits formed during the gradual deepening of the East Arm basin (Hoffman 1968). The Seton Formation basaltic to rhyolitic volcaniclastics, which have been dated by the SHRIMP U–Pb zircon method at 1883 ± 10 Ma (Van Breemen et al. 2013) and by CA-ID-TIMS at 1889.0 ± 0.7 Ma (Hoffman et al. 2023), are interbedded with the Kluzai and Akaitcho River formations of the Sosan Group, and the Gibraltar Formation of the lower Kahochella Group (Hoffman 1968; Van Breemen et al. 2013); therefore, GIF deposition corresponds in age with that for the 1889 Ma Seton Formation. The overlying McLeod Bay Formation is dominated by red, nodular shales and minor, dark green argillites, giving way to dark green, nodular argillites of the Charlton Bay Formation (Hoffman 1968). The Kahochella Group is overlain by the Pethei Group stromatolitic carbonate platform succession. The overlying, siliciclastic Christie Bay Group is marked by a change in paleocurrent direction from southwest to northeast, linked to the Hottah-Slave collision to the northwest (Van Breemen et al. 2013; Bowring and Grotzinger 1992; Hoffman et al. 2011).

3 | Description of Studied Material

3.1 | Lithology and Macroscale Textures

Outcrop samples were collected from two areas in the East Arm synclinorium: the Gibraltar Formation Type section area and Viren Island (described in Roscoe et al. 1987; locations are shown in Figure 1A and GPS coordinates for sample locations are listed in the Supporting Information). In the Type section area, samples were collected from the Type section (stratigraphic column in Figure 1C; samples labeled GIT-#) and from the poorly exposed lake shoreline outcrops along with Fe-rich stromatolites (samples labeled GIF-#) within ~1–2 km of the Type section. The exact stratigraphic position of these poorly exposed outcrops with respect to the Type section stratigraphy is uncertain. The base of the measured Type section hosts Fe-rich shales of the Gibraltar Formation that give way to interbedded GIF, shale, and carbonate. The contact with the underlying unit is submerged beneath the lake in this area and is not shown on the stratigraphic column (Figure 1C). The top of the Type section has carbonate and interbedded mafic tuffs interpreted to be derived from Seton Formation volcanic rocks. The contact with the overlying McLeod Bay is not present in the measured section. Another section was sampled from Viren Island (samples labeled GI-#), situated about 50 km northeast of the Type section area, placing it further from the inferred basin margin than the Type section (stratigraphic section shown in Figure S8). This section is thinner and has higher Fe content than the Type section. The lithologies sampled include GIF, Fe-rich shale, and Fe-rich carbonate; the latter two are referred to herein as silicate iron formation (SIF) and carbonate iron formation (CIF), respectively. GIFs contain medium to coarse sand-sized, Fe- and Si-rich grains, which often show oolitic texture, cemented by early diagenetic chert and dolomite, and lack aluminosilicate minerals (Figure 3B–E), consistent with their low [Al_2O_3] (Table S1). SIFs are thinly laminated, dominantly composed of clay minerals, and cemented by Fe oxide and carbonate minerals. CIFs are composed of massive dolomite and Fe-rich carbonate minerals with a significant clay mineral component.

Fe-rich, stromatolitic samples (Figure 3F–H) with alternating lamina of blobby hematite and chert-dolomite cement were found in the Type section area. Growth of stratiform mat laminae started on Fe-rich, sand-sized granular substrate (Figure 3G; apparent in the lowermost part of the photomicrograph). Microcolumnar stromatolitic texture gradually developed within the next 1–2 cm, evolving into well-developed columnar structures above. Columns are consistently ~1 cm wide, separated by ~0.1–0.3 cm of intercolumnar space. Column lamina are often linked across intercolumnar space but are occasionally interrupted with pieces of microbial mat ripups, granules of Fe oxides, and siliceous clasts filling intercolumnar space (Figure 3H).

3.2 | Petrography and Micropaleontology

Most commonly, grains in GIF samples contain a core of hematite that is coated with chert cortices tinted light red by microcrystalline dusty/microplaty hematite crystals, usually ranging in size from 1 to 10 μM (Figure 3C,D). Hematite crystals often form distinct concentric hematitic laminae, separating distinct Si-rich laminae, together constituting an oolitic texture. Some microplaty hematite crystals appear suspended within chert and are surrounded by cement, indicating that hematite predates cement precipitation. Where oolitic texture is not well preserved, grains appear broken or cracked, with Fe oxide minerals, and/or chert filling cracks (Figure 3C,D) or the chert phase filling voids in grains (Figure 3E). These Fe oxide mineral-filled cracks therefore postdate grain precipitation, infilling grain fractures that developed late in sediment burial. In some cases, grains retain an outer cortex of Fe oxide with fractures that are thoroughly impregnated with chert. GIF samples are largely devoid of siliciclastic material except for occasional clay minerals (< 1% by volume) between grains. Samples with high clay mineral content are not considered herein to reflect seawater composition.

Microfossils from the Gibraltar Formation are similar to the Gunflint biota and easily identified specimens are assigned to species initially described by Barghoorn and Tyler (1965). Fossil material is bright red to dark maroon and abundant in the hematite lamina, but difficult to observe where hematite crystals are densely packed. Morphology is more evident for specimens in the cement-rich lamina. The most common, easily distinguishable microfossils in the stromatolites are a spherical morphotype (Figure 4), resembling *Huroniospora macroreticulata* Barghoorn. The diameter of spherical

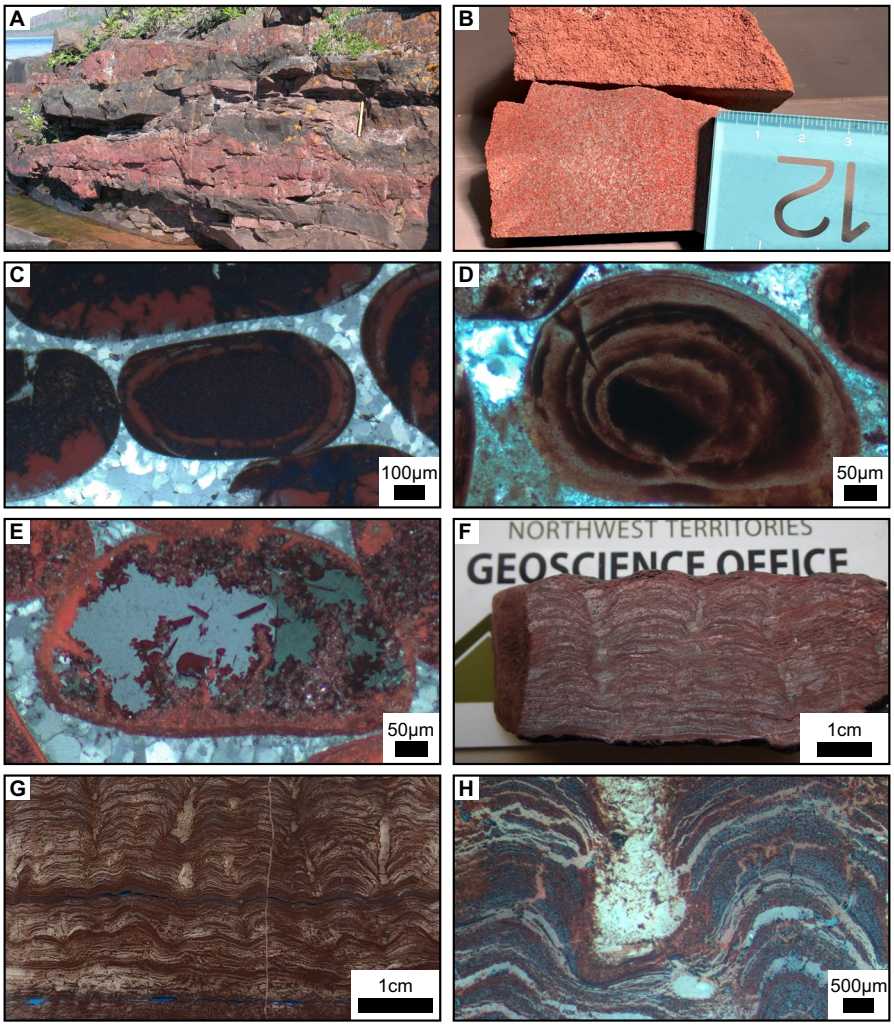

FIGURE 3 | (A) Outcrop, (B and F) hand sample, and (C–E, G, and H) thin-section photomicrographs of granular/oolitic iron formation and Fe-rich stromatolites. Note that chert cement filling intergranular space helped to protect grains from compression and dissolution. (C and D) Photomicrographs showing Fe-rich and Si-rich ooids. Grains with oolitic texture typically contain a massive, opaque, metallic hematite core. Ooids contain alternating Fe-oxide- and Si-rich lamina. Some Fe-oxide-rich lamina consist of massive, opaque, metallic hematite (C), whereas others contain tightly packed dusty hematite in a chert matrix (C and D). Silica-rich lamina usually contains dusty hematite, tinting the lamina dull maroon to bright red (C and D). Where primary, internal textures are overprinted, fine, bright-red, bladed, hematite crystals float in a cherty matrix (E). Fe-rich stromatolites contain interlaminated Fe-, Si-, or carbonate-rich lamina. (F) Photo of hand sample, (G) thin section, and (H) photomicrograph, showing columnar stromatolite with alternating Fe-oxide and Si-rich lamina, similar to that of Fe-rich oolitic granules. Stromatolite lamina developed on Fe-rich, sand-size granules is in the bottom ~0.5 cm of photomicrograph G.

microfossils ranges from 2.5 to 8.41 μm with a mean of 5.62 μm ($n = 88$). Some larger spherical microfossils show a rounded internal structure (Figure 4B).

The next most abundant specimen is a filamentous morphotype resembling *Gunflintia minuta* Barghoorn (Figure 5). Filaments are generally 0.5–1.5 μm in width with a mean width of 0.81 μm ($n = 11$) and up to 40 μm long. Filaments are straight or gently curved and do not show consistent orientation with respect to stromatolites in cross section. They can be found either in isolation or as randomly oriented clusters. Filaments occasionally display a twisted/coiled morphology, similar to that from the Gunflint Formation (Barghoorn and Tyler 1965; Cloud 1965) and some specimens show an attached rounded structure at one end of the filament (Figure 5B,C).

4 | Analytical Methods

4.1 | Sample Preparation and Elemental Analysis

Sample powders for geochemical analysis were prepared at the University of California, Riverside. Samples were cut and polished to remove any altered material and then washed using deionized water. Samples were subsequently pulverized to generate bulk-sample powder (passing 200 mesh sieve) for analytical work. Powdered samples were analyzed by Bureau Veritas. Bureau Veritas used lithium borate fusion dissolution and Aqua Regia digestion method prior to analysis by ICP-ES (emission spectroscopy) for major elements and ICP-MS (quadrupole mass-spectrometry) for trace elements. Detection limits for major elements were 0.01% except for Fe_2O_3, which had a detection limit of 0.04%. Detection

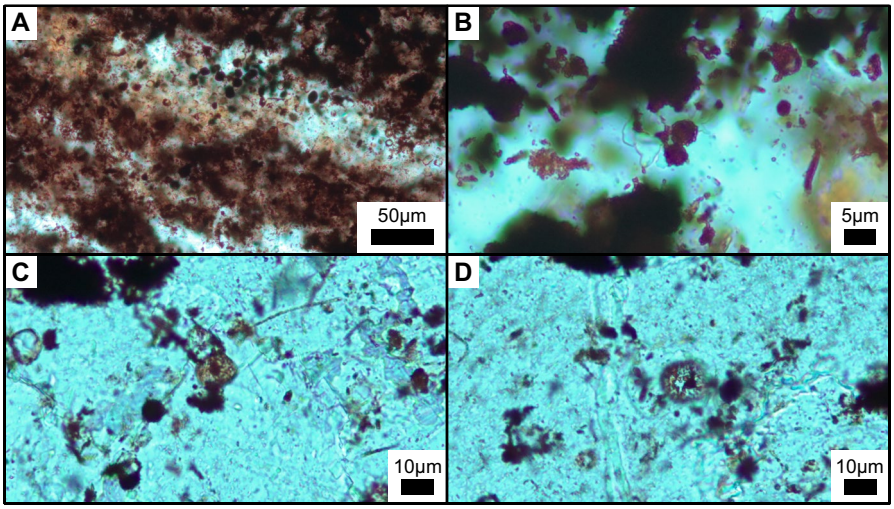

FIGURE 4 | *Spherical microfossils*. (A) Cluster of *H. macroreticulata* Barghorn in a hematite-rich stromatolite lamina. (B) High-resolution photomicrograph of two small *H. macroreticulata* Barghoorn in contact. (C and D) Larger spherical microfossils, with their internal structure revealed.

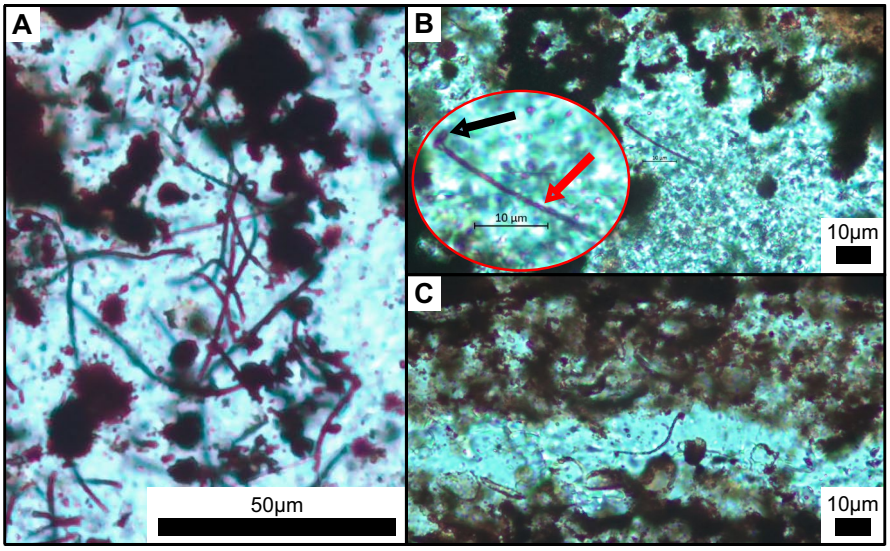

FIGURE 5 | *Filamentous microfossils*. (A) Cluster of filamentous *G. minuta* in Si-rich cement within stromatolite lamina. (B and C) Two specimens showing twisting along the length of the stalk and a rarely preserved rounded structure at one end of the stalk. In the oval inset in B, the specimen is shown enlarged. The black arrow points to the rounded structure, and the red arrow is pointing to the part of the stalk where twisted morphology is preserved.

limits for trace elements were 1 ppm or better except for Ni and V, which had detection limits of 20 and 8 ppm, respectively.

4.2 | Sm-Nd Isotope Analysis

Sample preparation and element separation for Sm–Nd isotope analyses of bulk-rock samples was carried out in PicoTrace clean lab facilities at Departamento de Geología (DG), Centro de Investigación Científica y de Educación Superior de Ensenada B.C. (CICESE), Mexico, following the procedure outlined by Weber et al. (2012). Isotope ratios were measured with a Nu-Instruments thermal Ionization Mass Spectrometer (Nu-TIMS) at DG, CICESE. Samarium and Nd were loaded on a double Re-filament arrangement in H_3PO_4. Measurements were performed in static mode on Faraday cups with 10^{11} Ω preamplifiers targeting ~1 V signal for ^{152}Sm and ~6 V signal for ^{144}Nd. For samples with Nd concentrations below ~8 ppm, masses 143–146 were measured on Faraday cups with 10^{12} Ω preamplifiers targeting for ^{144}Nd signal around 1 V. Reduction of the raw data was carried out offline with in-house developed Excel spreadsheets, in which data were corrected for isobaric interferences (^{144}Sm on ^{144}Nd and ^{150}Sm on ^{150}Nd using ^{147}Sm monitor during Nd analyses) and mass bias, using true $^{152}Sm/^{147}Sm$ and $^{146}Nd/^{144}Nd$ ratios, calculated from the natural $^{152}Sm/^{147}Sm$ (1.784535) and $^{146}Nd/^{144}Nd$ (0.7219) ratios, corrected for spike

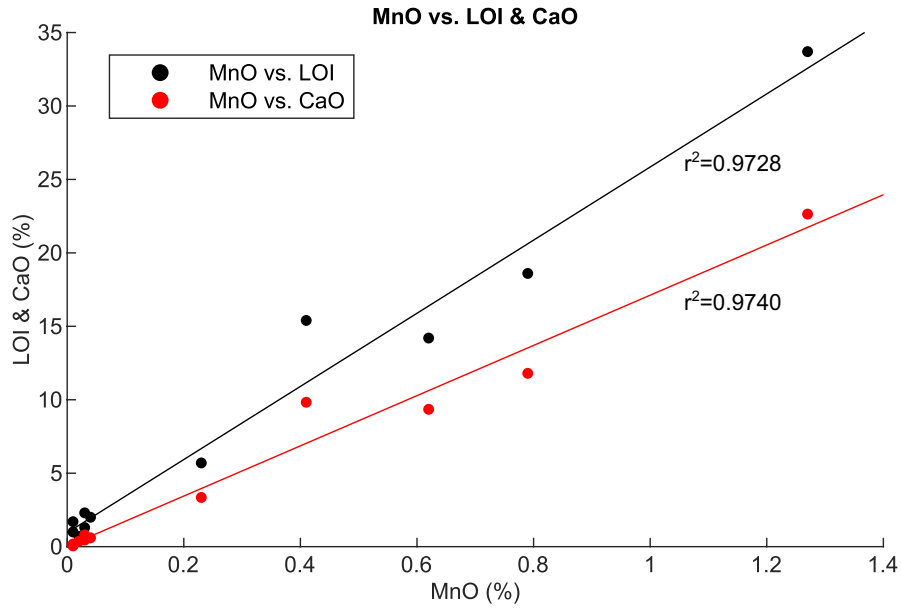

FIGURE 6 | Plots of MnO content versus LOI and CaO content demonstrating strong positive correlation, indicating that Mn is predominantly associated with carbonate minerals.

by iteration. Standards JNdi-1 and La Jolla (Tanaka et al. 2000), measured during the analytical sessions, yielded means of 0.512103 ± 0.000013 ($n=4$) and 0.511840 ± 0.000012 ($n=2$), respectively.

4.3 | Fe Isotope Analysis

Bulk-sample powders and powders produced from individual stromatolite lamina using a micromill were analyzed for Fe isotope composition. Sample preparation, Fe purification, and Fe isotope analysis were conducted for the bulk-sample powders at Origins Lab at the University of Chicago and for the micromilled sample powders of stromatolite lamina at Woods Hole Oceanographic Institution. Sample powders were digested using a $HF + HNO_3 + HClO_4$ mixture and then a $HCl + HNO_3 + HClO_4$ mixture in clean Savillex Teflon beakers. Digested samples were dried down and redissolved in 0.5 mL of 6 M HCl for Fe purification via established column chemistry procedures (for details, see Dauphas, Pourmand, and Teng 2009). Purified samples were dried and redissolved in 5 mL 0.3 M HNO_3 for analysis. Iron isotopic compositions were measured on a Neptune multi-collector inductively coupled plasma mass spectrometer (MC-ICP-MS) in medium-resolution mode at both institutions. Geostandards were processed using the same methodology and analyzed along with the samples to check that the procedure and measurement produce accurate results. Uncertainties are reported at the 95% confidence interval.

5 | Results

Major and trace element geochemical analyses were conducted on bulk GIF, SIF, and CIF samples. Iron isotopic analyses were conducted on both bulk-rock powders and individual micro-drilled GIF stromatolitic lamina and Sm-Nd isotopic analysis was conducted on bulk-rock powders. All geochemical data including major and trace element concentrations, Fe isotope values, Sm-Nd isotope values, and calculated anomalies and ratios are shown in Table S1 in the Supporting Information (see Supporting Information, Table S1 for the full dataset).

5.1 | Major and Trace Element Data

All samples in both sections are Fe rich. Total iron content, [Fe_2O_3], is between 4.5% and 12.0% in SIF samples, with one outlier in the Viren Island section at 44.2%, and 6.5% to 34.4% in CIF samples. Notably, [Fe_2O_3] is much higher in GIF samples from the Viren Island section, ranging from 32.5% to 46.2% (average = 39.5%), than from the Type section, which range from 7.8% to 34.4% (average = 14.9%). GIF samples contain low concentrations of elements associated with detrital aluminosilicate minerals. [Al_2O_3] ranges from 0.1% to 1.2% with one outlier containing 2.7% (GI-5). [K_2O], [TiO_2], and [Zr] are lower than 0.04%, 0.02%, and 10.9 ppm, respectively, in all GIF samples. Manganese content, [MnO], is below the detection limit (0.01%) for most GIF samples with Si-dominated cement. In GIF samples with [MnO] above the detection limit, [MnO] positively correlates with [CaO] ($r^2 = 0.97$) and LOI ($r^2 = 0.97$), indicating that carbonate cement hosts the majority of Mn. In four dolomite-rich GIF samples (including GIF-2-2, which hosts Fe-rich stromatolites), [MnO] is particularly high, ranging from 0.4% to 1.3%. CIF samples contain higher [Al_2O_3] than GIFs from 0.4% to 7.5% and the lowest [SiO_2] from 15.9% to 49.6%. SIF samples contain the highest [Al_2O_3] from 4.0% to 19.0% and [Zr] from 111 to 518 ppm. SIF and CIF samples in both sections also show a positive correlation between [MnO] and LOI (Figure 6), consistent with Mn being mostly associated with carbonate minerals.

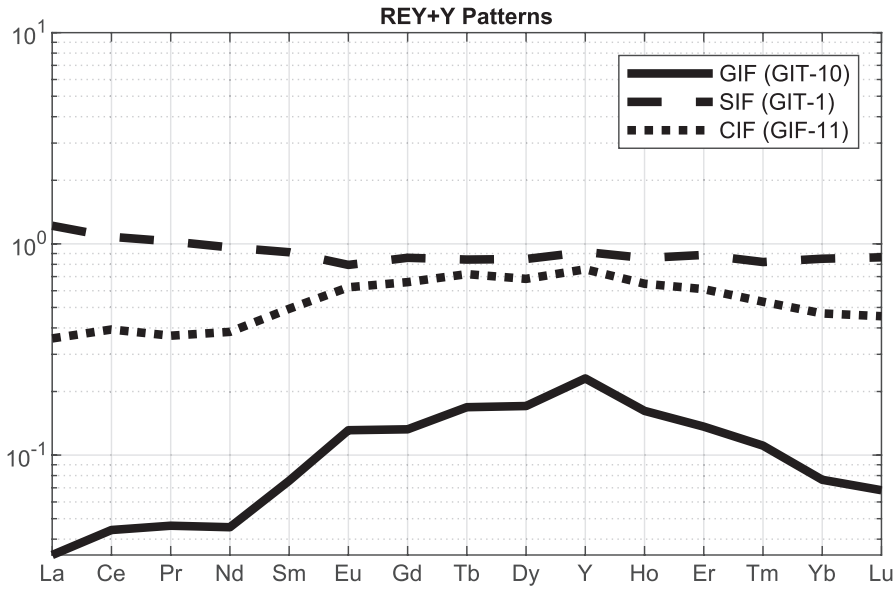

FIGURE 7 | PAAS-normalized REE+Y patterns for GIF, SIF, and CIF of the Gibraltar Formation. Three selected samples were plotted to show representative patterns for each sample lithology, however, there are significant differences in the patterns among samples of the same lithology. Note MREE hump shown by GIF and SIF samples.

5.2 | Rare Earth Elements + Yttrium Data

To screen samples for detrital contamination, we check for correlations among Al_2O_3 versus total REEs and Zr versus total REEs, for each lithology (Figures S1–S6). Regarding GIFs, Al_2O_3 and Zr show weak correlations with total REEs, with resulting r^2 values of 0.2 and 0.24, respectively. For SIFs, Al_2O_3 correlates with total REEs, whereas Zr does not, yielding r^2 values of 0.6 and 0.23, respectively. In the case of CIFs, both Al_2O_3 and less so Zr correlate with total REEs, with r^2 values of 0.72 and 0.38, respectively. Furthermore, we applied detrital corrections to GIF and CIF for REE+Y based on their Zr content and the average values for local shales (see Supporting Information and Table S2 for further details). However, these calculations resulted in anomalous outliers for some data points while minimally affecting others. Importantly, detrital-free GIF samples exhibit little to no change in REE+Y composition and anomalies after these corrections. We therefore do not incorporate these detrital corrections into the main text discussion. Instead, we exclude GIF samples GIF-2-2 and GI-1, SIF samples, and CIF sample GI-6 from paleoenvironmental interpretations due to their high Zr content (*SIF samples are included in data plots for reference*). Correlation plots and further details on the detrital correction calculations are available in the Supporting Information (Table S2).

REE+Y are herein normalized to Post-Archean Australian Average Shale (PAAS, denoted with subscript PAAS) values from Pourmand, Dauphas, and Ireland (2012). Lanthanum (La) anomaly was calculated using Pr and Nd as defined by Lawrence et al. (2006) to avoid using other anomalous REEs in the calculation. Ce anomaly was calculated using a Lagrangian extrapolation method, developed by Heard et al. (2022). The equations used to calculate LREE/HREE and Eu anomaly follow the conventional approach of Bau and Dulski (1996). The equation used to calculate MREE anomaly, after Chen et al. (2015), uses average LREE (La, Ce, Pr, and Nd), MREE (Sm, Eu, Gd, Tb, Dy, and Ho), and HREE (Er, Tm, Yb, and Lu) rather than only one representative element for each. The defining equations are

$$\text{La anomaly } (La/La^*_{PAAS}): \frac{[La]_{PAAS}}{\left([Pr]_{PAAS}{}^3/[Nd]_{PAAS}{}^2\right)} \quad (1)$$

$$\text{Ce anomaly } (Ce/Ce^*_{PAAS}): \frac{[Ce]_{PAAS}}{\left([Pr]_{PAAS}{}^{2.571}[Nd]_{PAAS}{}^{-1.931}[Sm]_{PAAS}{}^{0.360}\right)} \quad (2)$$

$$\text{LREE / HREE: } \frac{[Pr]_{PAAS}}{[Yb]_{PAAS}} \quad (3)$$

$$\text{Eu anomaly } (Eu/Eu^*_{PAAS}): \frac{[Eu]_{PAAS}}{\left(0.67[Sm]_{PAAS}+0.33[Tb]_{PAAS}\right)} \quad (4)$$

$$\text{MREE anomaly } (MREE/MREE^*_{PAAS}): \frac{2\Sigma[MREE]_{PAAS}}{\left(\Sigma[LREE]_{PAAS}+\Sigma[HREE]_{PAAS}\right)} \quad (5)$$

Eu anomaly was calculated using Sm_{PAAS} rather than Gd_{PAAS} since positive Gd anomalies are typical of seawater (De Baar, Brewer, and Bacon 1985). For the MREE anomaly, Ce^*_{PAAS} and Eu^*_{PAAS} are used in place of Ce_{PAAS} and Eu_{PAAS}, respectively, to avoid including anomalous values in the calculation. Spider diagrams of typical GIF, CIF, and SIF REE+Y patterns and results for the anomalies and ratio calculations are plotted in Figures 7 and 8, respectively. Ce, La, Eu, and MREE anomalies, and Y/Ho ratios are also shown stratigraphically for the Type section in Figure 9. Following the accepted practice, we refer to "positive" and "negative" REE_{PAAS} anomalies where values are >1 and <1, respectively. Eu/Sm vs. Sm/Yb is shown in Figure 10.

GIF samples feature both positive and negative Ce anomalies, LREE/HREE ratios mostly <1, and MREE enrichment. Their Y/Ho values are mostly above 27.2, the value for PAAS. The Viren Island and Type section GIF samples show similar REE+Y systematics, but the Viren Island section shows less variability. La anomaly values for GIF mostly scatter close to 1 with only two samples having significantly positive values in the Type section and one in the Viren Island section. Some GIF samples from the Type section show small positive Eu anomalies, whereas those from the Viren Island section are close to 1, and both sections have one sample each with a slightly negative Eu anomaly. While Y/Ho ratios are mostly above the chondritic value for GIF samples from the Type section, those from the Viren Island section are at or slightly below the chondritic value. CIF samples show far less variability in REE+Y than GIF samples. CIF samples do not show La, Eu, and Ce anomalies and have LREE/HREE ratios close to 1. Some CIF samples in each section have less pronounced MREE enrichment than GIF and some CIF samples from the Type section have a Y/Ho ratio above or below the chondritic average. SIF samples show largely flat REE+Y patterns (Figure 7) when normalized to PAAS with a slightly negative slope reflecting an enrichment in LREEs over HREEs. SIF samples also have LREE/HREE ratios slightly above 1, Y/Ho ratios near that for PAAS (~27.2), and no significant La, Ce, or MREE anomalies. A small negative Eu anomaly is shown by one SIF sample, but all other samples show no anomaly.

5.3 | Sm-Nd Isotope Composition

Samarium and Nd concentrations, calculated from isotope dilution analyses by TIMS, range from 0.15 to 1.99 ppm and 0.55 to 37.39 ppm for GIF samples, 1.33–2.49 ppm and 35.95–65.8 ppm for SIF samples, and 0.76–0.89 ppm and 11.14–20.56 ppm for CIF samples. Sm-Nd isotope composition, $\varepsilon_{Nd}(t)$ is reported as a ratio of radiogenic ^{143}Nd to stable ^{144}Nd in the sample relative to the chondritic uniform reservoir (CHUR, Bouvier, Vervoort, and Patchett 2008) at the time (t) when the sample started to behave as a closed system [$\varepsilon_{Nd}(t) = (^{143}Nd/^{144}Nd_{(t\text{-Sample})}/^{143}Nd/^{144}Nd_{(t\text{-CHUR})} - 1)\times 10^4$]. Screening for Nd isotope compositions of iron formation to infer seawater composition at the time of deposition requires stricter criteria than that for other seawater proxies. Since zircons could host exceptionally high concentrations of Sm and Nd, we exclude all samples with > 10 ppm Zr as well as all samples with > 1% Al_2O_3, establishing "detrital-free" and "detrital-rich" groups for the Type section and the Viren Island section. The $\varepsilon_{Nd}(1.89\,Ga)$ values of GIF samples from the Type section range from −3.9 to +1.29 compared to −5.17 to +2.12 for the Viren Island section. However, with data for the GI-1 sample

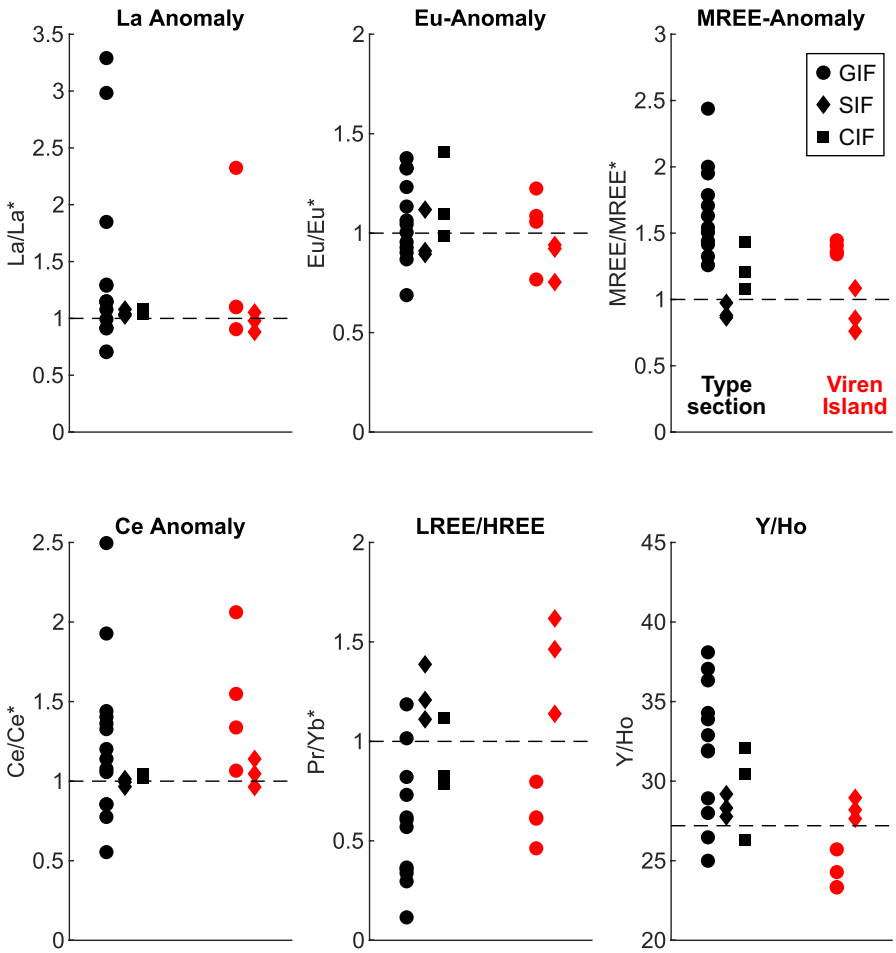

FIGURE 8 | REE+Y plots for the Gibraltar Formation showing La and Ce anomalies, LREE/HREE, Eu anomaly, and Y/Ho. The data are grouped horizontally by section (black—Type section; red—Viren Island section), whereas lithology is indicated by shape (circles—GIF, diamonds—SIF, and squares—CIF).

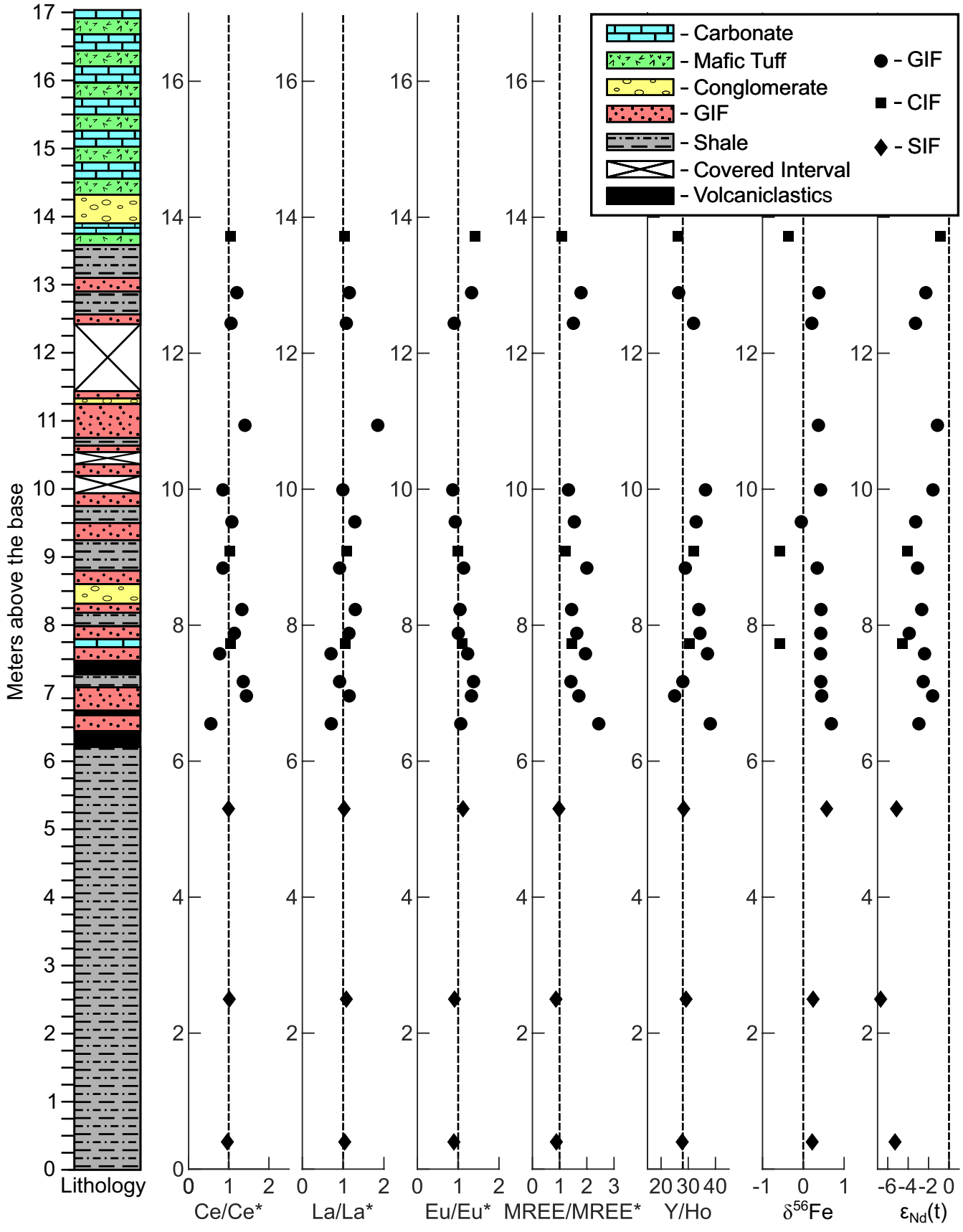

FIGURE 9 | Stratigraphic column of the Type section and the stratigraphic variations in La, Eu, MREE, and Ce anomalies, and LREE/HREE and Y/Ho with height in the Type section. Sample lithology is indicated by symbol shape (circles—GIF, diamonds—SIF, and squares—CIF).

from the Viren Island section excluded due to a high Zr content, the Viren Island GIFs have overall higher values ranging from −1.46 to +2.12. The ε_{Nd}(1.89 Ga) values of SIF samples from the Type section and the Viren Island section range from −6.7 to −5.14 and from −3.62 to +5.65, respectively. The ε_{Nd}(1.89 Ga) values measured for three CIF samples from the Type section are −4.59, −4.06, and −0.83 and one CIF sample from the Viren Island section has −5.79.

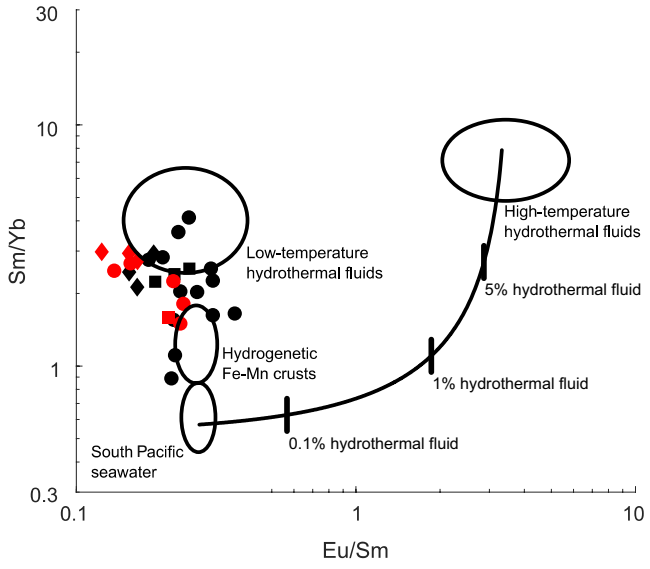

FIGURE 10 | Plot of Eu/Sm versus Sm/Yb for all Gibraltar Formation samples (after Alexander et al. 2008). Ranges are plotted for high-temperature hydrothermal fluids (Bau and Dulski 1996; Douville et al. 1999), low-temperature hydrothermal fluids (Michard et al. 1993), and shallow (< 500 m) North Pacific seawater (Alibo and Nozaki 1999). A two-component conservative mixing line is plotted from the shallow North Pacific seawater range to the high-temperature hydrothermal fluid range. Shown markers are for 0.1%, 1%, and 5% high-temperature hydrothermal fluid.

The Sm-Nd isotope data of 12 "detrital-free" samples plotted on an isochron diagram yielded a regression line that corresponds to a date of 1840 ± 90 Ma (total least squares) with an initial $^{143}Nd/^{144}Nd$ of 0.51014 (Figure S7), which corresponds to an ε_{Nd}(1.84 Ga) of −2.3 ± 1.7. The date overlaps with previous geochronological constraints for the Gibraltar Formation, implying that the Sm-Nd system has been closed since IF deposition and indicating that these values likely represent seawater composition in the East Arm basin during GIF deposition. Results for only "detrital-free" GIF samples from the Type section and Viren Island section are plotted on an $\varepsilon_{Nd}(t)$ vs. age plot (Figure 11) in black and red, respectively, along with a compilation of previously published $\varepsilon_{Nd}(t)$ values for IFs.

5.4 | Fe Isotope Composition

Detrital contamination screening for Fe isotope data follows that for REE+Y, described above. See Supporting Information for details regarding detrital correction for Fe isotope data. δ^{56}Fe values for both bulk-rock and micro-drilled stromatolite lamina are shown in Figure 12 and along the stratigraphic column for the Type section in Figure 9. The total range of δ^{56}Fe values for all measured samples is −0.58‰ to +0.73‰, similar to, but slightly lower than that for the Animikie basin GIFs (−0.35‰ to +0.81‰; Planavsky et al. 2009). GIF samples have the most positive values, followed by SIFs, and then CIFs (Figure 12A), and there is no statistically significant correlation among δ^{56}Fe values and any of the REE+Y proxies discussed above. For each lithology, Fe isotope values are overall higher in the Type section than in the Viren Island section. δ^{56}Fe values for individual, Fe-rich stromatolite lamina range from +0.35‰ to +0.63‰ with an

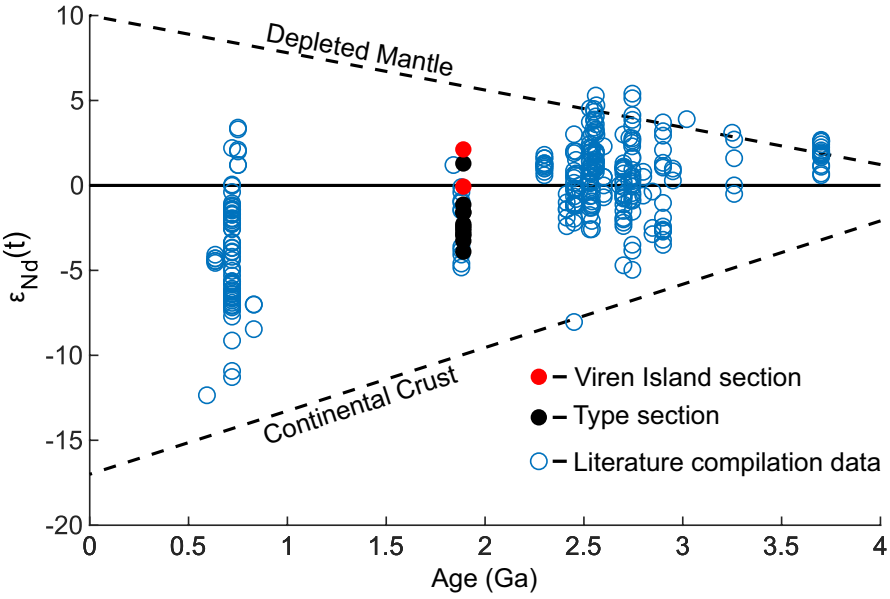

FIGURE 11 | Recent literature compilation of $\varepsilon_{Nd}(t)$ versus age. Data are compiled from recent compilations (Hu et al. 2020; Wang et al. 2022, 2024) and additional recent publications that were not included in these previous compilations (data and references are listed in Table S3). The data from sources that were not included in previous compilations were screened to select values, which are most likely to record seawater. Only samples with < 1% Al_2O_3 and < 10 ppm Zr were included. See the Supporting Information for references for all compilation data.

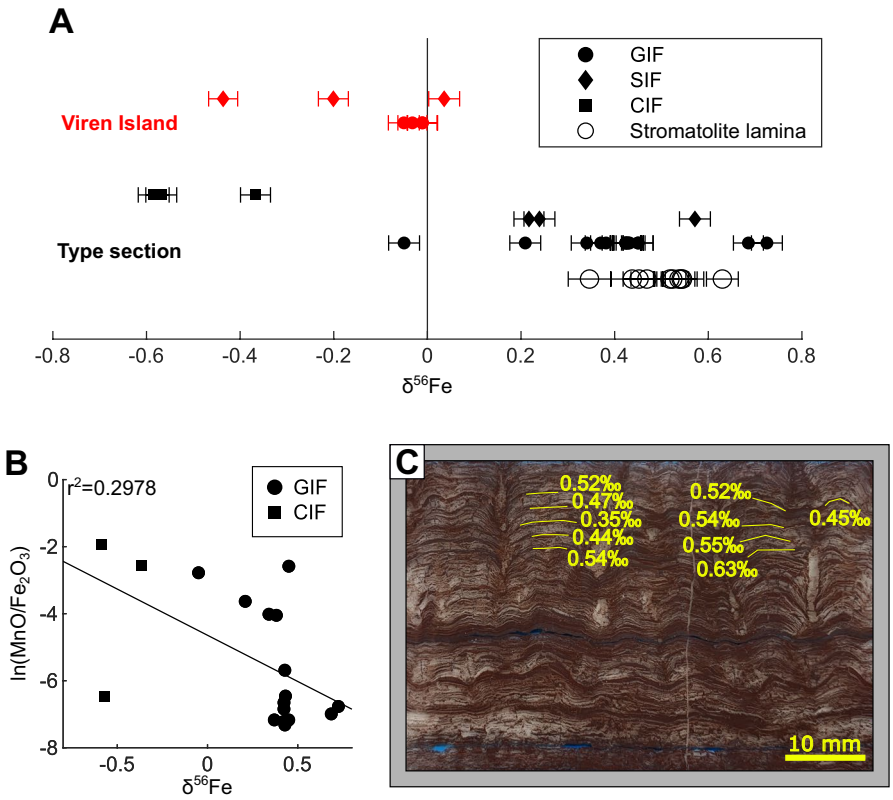

FIGURE 12 | Iron isotope composition of bulk-rock analyses from the Type and Viren Island sections and of micro-drilled stromatolite lamina from the Type section. (A) All Fe isotope data are grouped vertically by lithology. The Type section is shown in black symbols and the Viren Island section in red symbols. Lithology is indicated by shape (circles—GIF, diamonds—SIF, and squares—CIF), and the data for individual stromatolite lamina are shown with black open circles. (B) $\delta^{56}Fe$ vs. $\ln(MnO/Fe_2O_3)$ of detrital material-free GIF and CIF samples from the Type section showing a negative log-linear relationship. Location of micro-drilled lamina is shown in photo (C).

average of +0.50‰ (see Figure 12A; locations of micro-drilled lamina are shown in Figure 12B).

6 | Discussion

6.1 | Paleoenvironmental Setting of the East Arm Basin During GIF Deposition

The medium- to coarse-grained size of Fe-rich grains, absence of aluminosilicate (clay) minerals, presence of stromatolites with small column heights (< 1–2 cm), and lack of evidence for subaerial exposure in the studied GIFs are indicative of deposition in shallow water, regularly agitated, subtidal shoreface environments above the FWWB (about 10 m deep or shallower). Grains within the GIF often display oolitic texture (Figure 3C,D), aligning with deposition in a consistently wave-agitated setting. While diagenetic models have been proposed for granule formation in GIFs (Köhler et al. 2013; Dodd et al. 2018), the oolitic texture of the Gibraltar Formation GIF is reminiscent of that observed in carbonate ooid cortices that formed in wave-agitated environments (Trower, Lamb, and Fischer 2017). Although often disturbed, deformed, and broken, oolitic cortices are delicately preserved in many granules and otherwise resemble the texture of the stromatolite lamina in the same unit. The stromatolites have continuous laminae only rarely interrupted where two columns meet and lack coarse grains relative to GIF samples, indicating that they likely developed in areas with calmer waters, less disturbed by wave activity than settings where Fe-coated grains were deposited. With sedimentological evidence suggesting that these GIFs were deposited in shoreface environments, REE+Y provides additional insight into biogeochemical processes in the basin.

The La anomaly can serve as a proxy for the degree of connection between the basin and the open ocean. Positive La anomaly is a characteristic linked to differing organic complexation relative to neighboring REEs (De Baar, Schijf, and Byrne 1991) and partial REE+Y scavenging onto Fe oxyhydroxides (Bau 1999; Bau and Koschinsky 2009). It is typically developed in seawater (Bau and Dulski 1996) but is absent from freshwater lakes and rivers (Kulaksız and Bau 2011). Positive La anomaly is mostly absent in the Gibraltar Formation samples (Figure 7A). Some GIF samples display positive La anomaly, consistent with at least partial, perhaps varying, connection to the open ocean for the East Arm basin. In a partially restricted basin, terrestrial waters may exert a significant influence on water composition and mixing between terrestrial and marine waters could contribute to variability in geochemical proxies, resulting in an overall attenuation of seawater signature.

Despite likely basinal restriction and mixing of terrestrial and marine waters, some small positive Eu anomalies (Figure 8B) are present in the Gibraltar Formation. These values potentially point to a supply of high-temperature hydrothermal fluids to the basin (Sverjensky 1984; Michard et al. 1993). Positive Eu

anomalies are typical of nearly all Archean and Paleoproterozoic IFs. Compilations of Eu anomalies normalized to PAAS in IFs have shown a range of 0.36–6.4 with a mean of 1.74 for the pre-GOE, Archean to early Paleoproterozoic IFs, and a range of 0.98–2.44 with a mean of 1.48 for the late Paleoproterozoic, ca. 1.88 Ga IFs (Planavsky et al. 2010; Wang et al. 2023). The values for the ca. 1.89 Ga Gibraltar Formation range from 0.66 to 1.32 with an average of 1.01, which are similar to, but significantly lower than those previously calculated for GIFs of the same age. Small positive Eu anomalies are also present in the ca. 1.88 Ga Frere Formation and Animikie basin GIFs (Planavsky et al. 2010).

Spatial variation in Eu anomalies in the Gibraltar Formation GIFs lends further support to the argument for a deep-water, high-temperature hydrothermal source of Fe to the basin. Positive Eu anomalies in the Gibraltar Formation are exclusively found in GIFs from the Type section, which during deposition was located closer to the inferred basin connection to the open ocean than the Viren Island section based on paleocurrent indicators (Hoffman 1968). Various processes could have contributed to a decrease in the magnitude of positive Eu anomaly in the Fe-rich waters as they expanded into the basin. Detrital sediments and terrestrial waters from shale and granite-rich hinterlands could carry negative Eu anomaly (Condie 1993; Gao and Wedepohl 1995) and would dilute positive Eu anomaly of high-temperature hydrothermal fluids in a shoreface environment. Positive Eu anomalies progressively decrease with distance from a hydrothermal plume origin as Eu is removed from hydrothermal fluids via particle scavenging disproportionately faster with respect to its neighboring REE because this scavenging process is proportional to REE concentration (Olivarez and Owen 1991). In the Type section, the most positive Eu anomalies occur in GIF immediately above or below volcaniclastics in the lower part of the section. This might be taken as a further indication of association with volcanism; however, the Eu anomaly does not increase in GIF toward mafic tuffs in the upper part of the Type section. The magnitude of positive Eu anomaly (Figure 8B) might therefore reflect the relative proximity of the sections to the open ocean. Being further from the open-marine setting, the positive Eu anomaly for the Viren Island section might have been more diluted by terrestrial waters and/or detrital contamination.

In mixing calculations between seawater and high-temperature hydrothermal fluids, hydrothermal fluids are only necessary in small quantities to develop the REE+Y patterns observed in ancient IF (Khan et al. 1996; Alexander et al. 2008). Figure 10 shows Eu/Sm vs. Sm/Yb for the Gibraltar Formation and other ca. 1.88 Ga GIFs, along with general ranges for seawater, high- and low-temperature hydrothermal fluids, hydrogenetic Fe–Mn crusts, and a conservative mixing line between seawater and high-temperature hydrothermal fluids. The graph demonstrates that a high-temperature fluid–to-seawater ratio of less than 1:1000 is necessary to explain the Eu/Sm values for the Gibraltar Formation. Furthermore, high Sm/Yb points toward low-temperature hydrothermal fluids, which carry neutral or weak positive Eu anomalies (Michard et al. 1993).

In addition to REE+Y, Sm-Nd isotope systematics can be used to trace the source of chemical sedimentary rock constituents. Sm and Nd partition differently between the Earth's mantle and crust (DePaolo 1980), whereby Nd is an incompatible lithophile element that is preferentially partitioned into melt in igneous systems, while Sm is more compatible with mafic mineral characteristics of the mantle. Since ^{147}Sm decays to radiogenic ^{143}Nd, the mantle has become enriched and the continental crust depleted in ^{143}Nd relative to the Chondritic Uniform Reservoir (CHUR) over geological time, resulting in isotopically distinct juvenile, depleted mantle and evolved, continental crust arrays that have progressively diverged through time (Figure 11). The Nd isotopic composition of the provenance could be transferred to sedimentary systems when the source rock is weathered and ultimately recorded by chemical sediments, which reflect the isotopic composition of ambient waters from which they precipitated (Piepgras and Wasserburg 1985; van de Flierdt et al. 2016). Similarly, hydrothermal fluids that leached juvenile seafloor basalts also influence the Nd isotopic composition of seawater (Piepgras and Wasserburg 1985). Although the Nd isotope composition of modern seawater is dominantly influenced by continental weathering sources (van de Flierdt et al. 2016), many studies have demonstrated that seawater recorded by ancient IFs was significantly influenced by hydrothermal fluids (see Figure 11 and supplementary references for compilation of Sm-Nd isotope data for IF through geologic time). A major advantage these measurements have over the Eu anomaly is that they reflect the relative contribution of hydrothermally derived, juvenile REE+Y to continentally derived, evolved REE+Y irrespective of the temperature of hydrothermal fluids (McCulloch et al. 1981; O'Nions et al. 1978). The Sm-Nd isotope systematics has therefore long been used in studies of ancient chemical sedimentary rocks as a tracer of dissolved solute fluxes to seawater to differentiate between continental weathering and hydrothermal sources (Miller and O'Nions 1985; Jacobsen and Pimentel-Klose 1988). However, since the $\varepsilon_{Nd}(t)$ of sedimentary rocks depends fundamentally on the age and the Sm/Nd of their source rocks, weathering juvenile continental source rocks can generate the same $\varepsilon_{Nd}(t)$ values as those of hydrothermal fluids that altered juvenile seafloor basalts. The $\varepsilon_{Nd}(t)$ values therefore should be considered alongside other available proxy data that might help to distinguish between these two options.

The ε_{Nd}(1.89 Ga) values for "detrital-free" samples from the Gibraltar Formation are similar to those from other ca. 1.88 Ga GIFs measured to date (Figure 11). The initial ^{143}Nd/^{144}Nd of the regression line (0.51014; Figure S7) is not as radiogenic as expected for hydrothermal fluids that obtained Nd from mantle-derived magmas at the time of deposition, indicating that the Nd isotope composition of seawater at the site where the Gibraltar Formation GIF was precipitated was not entirely dominated by juvenile, hydrothermal input. A significant amount of evolved Nd, likely delivered from old continental crust to the basin, is necessary to explain the slightly negative ε_{Nd} values in "detrital-free" samples.

The Sm-Nd isotope record (Figure 11) shows a well-developed juvenile hydrothermal signature for Archean and early Proterozoic IFs, but values for the Gibraltar Formation and other ca. 1.88 Ga GIFs are more consistent with either a dominant source of sediments and waters from a relatively young terrestrial provenance or mixing of evolved, terrestrial sources with hydrothermally influenced seawater. Considered alongside the small positive Eu anomalies and insights of the Eu/Sm versus Sm/Yb graph discussed above, the intermediate $\varepsilon_{Nd}(t)$ values for the Gibraltar Formation (Figure 11) between those of depleted mantle and evolved, continental crust are best explained by source mixing

between an Fe-rich, juvenile hydrothermal fluids, which had a significant low-temperature component, and terrestrial groundwater and riverine waters.

Positive MREE anomalies in IFs are a topic of discussion (e.g., Alexander et al. 2008). MREE enrichment, known as an MREE arch or bulge for the hat shape in REE+Y patterns (apparent in GIF and Type section CIF samples of the Gibraltar Formation; Figure 8C), is present in modern river waters (Hannigan and Sholkovitz 2001). Alexander et al. (2008) speculated that the ca. 2.9 Ga Pongola Supergroup IFs are MREE-enriched due to a significant flux of MREE-enriched river water. For the Gibraltar Formation, larger MREE anomalies in the Type section area than those from the Viren Island section are inconsistent with a riverine source hypothesis since the Type section was farther from the shore. MREE enrichment is particularly common in Phanerozoic fossiliferous phosphorites and has been linked to early diagenesis (Chen et al. 2015). However, the Gibraltar Formation GIFs contain very low to negligible amounts of phosphorus, and no correlation is noted between [P] and MREE anomaly. MREE enrichment is also common in Paleoproterozoic carbonate successions and has been attributed to redox cycling of Fe oxyhydroxide minerals in the water column (Hodgskiss et al. 2021). It has also been demonstrated that MREE enrichment develops in ferruginous pore waters during early diagenesis (Haley, Klinkhammer, and McManus 2004) and might result from the redox cycling of Fe oxyhydroxides in the water column (Bellefroid et al. 2019). It seems most likely that MREE enrichment observed in the Gibraltar Formation GIFs might also be related to the development of MREE enrichment in ferruginous porewaters due to Fe oxyhydroxide redox cycling.

Due to the different redox-sensitive particle reactivity of Ce, LREE, Y, and other REE, Ce anomaly, LREE/HREE, and Y/Ho can be useful indicators of redox conditions. Ce anomaly for GIF samples (Figure 8D) ranges from positive to slightly negative. GIFs and CIFs are predominantly LREE depleted (Figure 8E). Ce anomalies and LREE/HREE are consistent with Fe and Mn cycling across a redoxcline poised above the storm wave base and likely above the FWWB. Similarly, the subchondritic Y/Ho values (Figure 8F) for GIF samples are best explained by Fe–Mn oxyhydroxide dissolution, preferentially releasing Ho below the redoxcline. Considered qualitatively, these values support the existence of a shallow redoxcline, maintaining ferruginous deep waters below at least slightly oxygenated surface waters. As with La and Eu anomalies, the larger variability in the redox-sensitive REE+Y proxies in the Type section than in the Viren Island section might be explained by more pronounced redoxcline fluctuation and mixing of waters near the access to the open ocean.

6.2 | Iron Isotope Constraints on Basinal Redox and Fe Cycling

GIF samples GIF-2-2 and GI-1, SIF samples, and CIF sample GI-6 are not considered to reflect seawater Fe isotope composition as they contain a large detrital component (SIF samples are included in data plots for reference). While the REE+Y composition of GIFs is sensitive to environmental factors, including detrital contamination, riverine water contribution, and Fe–Mn oxyhydroxide cycling, δ^{56}Fe values of GIFs provide more direct insight regarding the mechanisms involved in Fe cycling from the source to the sink. High-temperature hydrothermal fluids have δ^{56}Fe values of $Fe^{2+}_{(aq)}$ ranging from −0.7‰ to 0.0‰ (Rouxel et al. 2008). Alternatively, an organically complexed (chelated) continental source of Fe, during time periods of enhanced weathering, is often considered for Phanerozoic ironstones (see Bekker and Kovalick 2021 for further discussion). Fluvially transported Fe shows a large range in Fe isotope values, from −1.4‰ to +1.83‰ in the Lena River basin for example (Hirst et al. 2020), bracketing the continental crust composition at ~0‰ (cf. Poitrasson 2006; Gong et al. 2017). While our Fe isotope data do not resolve between hydrothermal, deep ocean versus continental Fe fluxes alone, combined with positive Eu anomalies and lighter Fe isotope values in the Viren Island section, which was more distal to the open ocean with respect to the Type section, they are most consistent with a submarine hydrothermal source. As another alternative, isotopically light, terrestrial $Fe^{2+}_{(aq)}$ source, driven by microbial dissimilatory Fe^{3+} reduction (DIR) of Fe oxyhydroxides in sediments, has also been considered (Severmann et al. 2008). DIR produces low δ^{56}Fe values in the $Fe^{2+}_{(aq)}$ product of reductive dissolution, approximately 3.0‰ lighter than the source sediments (Severmann et al. 2010), however, it is difficult to uniquely identify DIR-derived Fe sources in palaeoceanographic settings.

Alternatively, an input δ^{56}Fe value of ~0‰, associated with a hydrothermal Fe source, can satisfy the measured values for GIFs. This interpretation gains some support from the associated positive Eu anomalies since these are only developed at the Type section, which was closer to the open ocean than the Viren Island section. This suggests a loss of positive Eu anomaly in the hydrothermally influenced waters as they expanded into the basin. The difference in δ^{56}Fe values between the two sections further supports this interpretation. As Fe-rich fluids travel away from their source, partial Fe oxidation preferentially removes heavy Fe isotopes, leaving the residual $Fe^{2+}_{(aq)}$ in solution relatively enriched in light Fe isotopes, resulting in lower δ^{56}Fe values. Lower δ^{56}Fe values in the Viren Island section relative to the Type section, along with a total range of Fe isotope values of ~0.8‰ in GIFs, are therefore best explained by a varying degree of partial Fe oxidation of upwelling, hydrothermally influenced deep waters at the depositional site, accompanied by a fractionation factor between 1.0‰ and 1.5‰. Partial Fe oxidation has been observed for spontaneous abiotic ferrihydrite precipitation (Bullen et al. 2001), adsorption and precipitation of Fe onto cyanobacterial cell surfaces (Mulholland et al. 2015), microbially mediated photo-oxidation by photoferrotrophs (Croal et al. 2004; Swanner, Wu et al. 2015), microbially mediated oxidation fueled by nitrate reduction (Kappler et al. 2010), and direct microbial oxidation by chemolithotrophic FeOB (Balci et al. 2006).

Rayleigh distillation for Fe isotopes of Fe oxyhydroxide precipitate ($\delta^{56}Fe(III)_{ox}$) from an initial δ^{56}Fe value of Fe^{2+} in solution ($\delta^{56}Fe(II)_i$) with a fractionation factor, ε, of 1.5‰ can be evaluated using the following equation:

$$\delta^{56}\mathrm{Fe(III)}_{\mathrm{ox}} = \delta^{56}\mathrm{Fe(II)}_{\mathrm{i}} - \varepsilon \ln(f)\left(\frac{f}{1-f}\right) \quad (6)$$

where f is the fraction of $Fe^{2+}_{(aq)}$ remaining in solution. Applying this equation using the lower bound of δ^{56}Fe values

for the hydrothermal source ($\delta^{56}Fe(II)_i = -0.7‰$), $\delta^{56}Fe(III)_{ox}$ values of GIF samples from −0.05‰ to +0.73‰ (Figure 12A) can be reproduced with f ranging between 0.23 and 0.91. On the other hand, for the upper bound ($\delta^{56}Fe(II)_i = 0.0‰$), no more than 27.5% (i.e., $f < 0.28$) of $Fe^{2+}_{(aq)}$ would have been left in solution to generate the maximum $\delta^{56}Fe(III)_{ox}$ value (0.73‰) for Fe oxyhydroxide precipitate. While quantitative oxidation may account for some GIF $\delta^{56}Fe(III)_{ox}$ values, a varying degree of partial oxidation is still necessary to explain values above 0‰. Furthermore, a negative log-linear relationship observed between $\delta^{56}Fe$ values and Mn/Fe for detrital-free bulk-rock analyses for the Type section (Figure 12B), as observed in other post-GOE GIFs (Wang et al. 2023), supports this interpretation, as this trend is expected for fluids upwelling into oxic shallow waters with preferential oxidative removal of iron with heavy isotopes (Tsikos et al. 2010; Planavsky et al. 2014; Hiebert et al. 2018; Nie et al. 2020).

These findings support the interpretation by Planavsky et al. (2009), who also inferred partial Fe oxidation for the Fe isotopic signature of GIFs and Fe-rich stromatolites from the Gunflint Formation based on bulk-rock analyses. Combined, these two studies suggest that the deposition of ca. 1.88 Ga GIFs broadly followed a similar pathway, genetically tied to partial biological Fe oxidation by FeOB. In contrast, Heard et al. (2022) suggested, based on a narrow range in Fe isotope composition of both bulk-rock and individual stromatolite lamina of Fe-rich stromatolites of the ca. 2.46–2.43 Ga Griquatown Iron Formation GIFs, that $Fe^{2+}_{(aq)}$ proximal to the stromatolites was quantitatively oxidized by oxygen produced by cyanobacteria in the stromatolites. The total range of about 0.8‰ for bulk-rock $\delta^{56}Fe$ values of the Gibraltar Formation GIFs is much larger than that of ~0.1‰ for the Griquatown Iron Formation GIFs (Heard et al. 2022). Results of microanalysis of individual stromatolite lamina from the Gibraltar Formation Fe-rich stromatolites (Figure 12) also contrast with those for the Griquatown Iron Formation, displaying a wider range of Fe isotope values in a smaller sample population (0.35‰–0.63‰; $n = 10$). Moreover, these values are among the heaviest measured in bulk-rock analyses, indicating that Fe oxidation in stromatolites was partial rather than quantitative.

6.3 | Comparing the Biological Affinity and Ecology of Microfossils From the Gibraltar Formation With Ecosystems Thriving in Modern Ferruginous Settings

Abundant filamentous and spheroidal microstructures in GIF-hosted, Fe-rich stromatolites of the Gibraltar Formation (Figures 4 and 5) closely resemble microfossils observed in other ca. 1.88 Ga GIFs (Barghoorn and Tyler 1965; Cloud 1965; Knoll and Simonson 1981; Walter, Goode, and Hall 1976). To address the sedimentary origin and biogenicity of the microstructures, we consider their relationship to mineralogical and textural rock components and their general morphology. The microstructures appear to predate any cross-cutting fractures and veins in the chert-dolomite cement. Microstructures occur only in columnar stromatolite samples, within convex stromatolite column lamina and were not found occurring in the intercolumnar space. The size of filamentous specimens is consistent with that of the modern FeOB Zetaproteobacteria *Mariprofundus ferrooxydans* and the size of spherical specimens is consistent with numerous globular, single-celled microorganisms. Neither microfossil morphology shows any spatial trend beyond their higher abundance near the apex of stromatolite lamina. No organic matter was found preserved in microfossils in stromatolite samples, indicating that any organic matter that was initially present was fully oxidized and replaced by micro-crystalline hematite shortly after deposition, prior to chert-dolomite cement precipitation. Additionally, Fe biomineral stalks produced by FeOB contain low organic carbon relative to Fe content (Bennett et al. 2014), which could also explain the lack of organic matter. Despite the replacement of original organic matter, these observations support a sedimentary and biogenic origin for the morphology of these structures.

Different interpretations have been proposed for the biological affinity of microfossils of the Gunflint biota. While earlier work heavily hinged on a cyanobacterial affinity, with some suggestions that they could represent early eukaryotes (Barghoorn and Tyler 1965; Cloud 1965; Knoll and Simonson 1981; Walter, Goode, and Hall 1976), later work favored a prokaryotic origin for these microfossils (Awramik and Barghoorn 1977). The two most common and least enigmatic members of the Gunflint biota are a globular form, *Huroniospora macroreticulata* Barghoorn, and a filamentous form, *Gunflintia minuta* Barghoorn (Barghoorn and Tyler 1965). Some filamentous forms have been noted to look twisted along their length (Barghoorn and Tyler 1965; Cloud 1965). This morphology was compared to modern *Cyanobacteria Spirulina*, which grows naturally coiled organic filaments (Castenholz 1969) and modern FeOB strains, which extrude an Fe oxyhydroxide stalk from their cell as a waste product of their Fe oxidizing metabolism (Emerson et al. 2007; Chan et al. 2011). The FeOB cell rotates as it extrudes its stalk, developing the characteristic twisted morphology (Chan et al. 2016).

The two most common morphotypes in the Gibraltar Formation stromatolites are the globular (Figure 4) and filamentous (Figure 5) forms identified as *Huroniospora macroreticulata* and *Gunflintia minuta*, respectively, following the nomenclature of the Gunflint biota (Barghoorn and Tyler 1965). Specimens of *G. minuta* in the Gibraltar Formation stromatolites occasionally show a twisted morphology along their length, as noted in previous studies. Some rare specimens display an attached structure at one end of the filament (Figure 5B,C), resembling a cell and biomineral stalk of the modern FeOB *Mariprofundus ferrooxydans*. At the redoxcline developed in the East Arm basin, the confluence of $Fe^{2+}_{(aq)}$ upwelled from ferruginous deep waters and dissolved $O_{2(aq)}$ in oxygenated shallow waters would have created optimal conditions for FeOB. In contrast, for many cyanobacteria species it has been demonstrated that high $Fe^{2+}_{(aq)}$ concentrations could be toxic (Swanner, Mloszewska et al. 2015; Rantamäki et al. 2016). In lab culturing of *Synechococcus* PCC 7002, Swanner, Mloszewska et al. (2015) found that in a growth medium with $[Fe^{2+}_{(aq)}]$ over 180 μM, cyanobacterial growth was severely stunted. Once intercellular reactive oxygen species developed in response to increased $Fe^{2+}_{(aq)}$ concentrations, the overall efficiency of oxygenic photosynthesis declined. Environments co-inhabited by FeOB may further exacerbate this limitation for cyanobacteria. A recent study shows that some FeOB can prolong their ability to outcompete abiotic Fe oxidation by secreting an exometabolome that increases the

residence time of $[Fe^{2+}_{(aq)}]$ in the presence of O_2 by up to 100-fold (Baker et al. 2023).

Although there are no modern environments directly equivalent to GIF-depositing basins, FeOB do commonly occupy spatially restricted environments near $Fe^{2+}_{(aq)}$ sources, including hydrothermal vents like those at Kama'ehuakanaloa seamount (formerly Lō'ihi seamount; Emerson and Moyer 2002), anoxic groundwater seeps (Krepski, Hanson, and Chan 2012), and acid mine drainage (Johnson et al. 2002). At Kama'ehuakanaloa, stalk-forming FeOB are found forming microbial mats, growing aligned toward increasing O_2 along an $Fe^{2+}_{(aq)}$–$O_{2(aq)}$ gradient (Chan et al. 2016). However, in Nagahama Bay in Kagoshima, Japan, where Fe-rich fluids emanate from hydrothermal vents, *Mariprofundus ferrooxydans* grows in random orientation in Fe oxyhydroxide chimney mounds (Kiyokawa et al. 2021). The random orientation of the filaments in the Gibraltar Formation stromatolites most closely resembles modern FeOB growing in Nagahama Bay. Similarities with modern examples demonstrate that these organisms occupied a similar niche in the late Paleoproterozoic as they do today. Although microfossils in the ca. 1.88 Ga GIFs are not the oldest to be interpreted as FeOB, the pre-GOE record of possible FeOB microfossils is sparse and uncertain (Dodd et al. 2017; Little et al. 2021). We next consider if this might be related to a less common expression of FeOB-preferred biogeochemical conditions, which involve a delicate balance between $[Fe^{2+}_{(aq)}]$ and $[O_{2(aq)}]$ in settings such as shoreface environments on continental shelves where they are more likely to be preserved.

6.4 | Fe Oxyhydroxide Precipitation Fueled by a Balance Between an Aqueous Fe^{2+} Source and Ambient Atmospheric O_2 Concentration

Our findings from the Gibraltar Formation align with the interpretation that favorable $[Fe^{2+}_{(aq)}]$ and $[O_{2(aq)}]$ for the FeOB metabolism were geographically widespread in GIF-forming environments. High $[Fe^{2+}_{(aq)}]$ concentrations also likely stifled local oxygen production by cyanobacteria beneath the redoxcline, situated at or even above the FWWB. While cyanobacteria likely did not face similarly extreme challenges above the redoxcline, their growth may have been locally hindered by enhanced upwelling of Fe-rich deep waters and FeOB secreting an exometabolome (Baker et al. 2023), which helped to maintain Fe-rich conditions above the redoxcline, thus curtailing cyanobacterial O_2 production in these environments. Locally developed Mn enrichments and stromatolite morphology, however, indicate cyanobacterial influence, at least locally and episodically, above the redoxcline, in the shallow-water, subtidal to intertidal settings. In the absence of substantial local O_2 production, a major source of $[O_{2(aq)}]$ for FeOB would likely have been exchange between the atmosphere and seawater. We therefore use inferred values for $[Fe^{2+}_{(aq)}]$ in upwelling, deep waters sufficient for the deposition of IFs (Holland 1973; Morris 1993; Thompson et al. 2019), combined with FeOB metabolic requirements, to constrain the atmospheric pO_2 at which FeOB would bloom in shoreface settings where local cyanobacterial O_2 production was limited. These calculations, serving as a maximum bound for atmospheric pO_2 during this ca. 1.88 Ga GIF deposition event, represent the first estimates rooted in microbial metabolism.

To determine the biogeochemical conditions that would place the redoxcline at or above the FWWB, satisfying sedimentological and geochemical constraints of the Gibraltar Formation GIFs, and combined O_2 and $Fe^{2+}_{(aq)}$ requirements of microaerophilic FeOB (Chan, Emerson, and Luther 2016), we calculate the range of $[O_{2(aq)}]$ in wave-agitated, shallow waters for a range of $[Fe^{2+}_{(aq)}]$ in upwelling, ferruginous waters that would set the redoxcline at 10-m deep or shallower. We adapt an equation from a simple 1D model used by Heard et al. (2020) for the depth of the redoxcline ($z_{redoxcline}$) for a given $[O_{2(aq)}]$ above the redoxcline, which in this case represents surface waters in equilibrium with the atmosphere ($[O_{2,\,surface}]$), and a given maximum $[Fe^{2+}]$ in deep waters prior to upwelling and oxidation ($[Fe^{2+}_{deep}]$):

$$z_{redoxcline} = z_{model} - \frac{z_{model}}{\left(1 + \left(\frac{4[O_{2,\,surface}]}{[Fe^{2+}_{deep}]}\right)\right)} \quad (7)$$

where z_{model} is the depth scale over which Fe upwells and is oxidized; we estimate it to be on the order of the depth of the continental shelf. This equation can be rearranged to calculate $[O_2]_{surface}$:

$$[O_{2,\,surface}] = \left(\frac{z_{model}}{z_{model} - z_{redoxcline}} - 1\right) \times \frac{[Fe^{2+}_{deep}]}{4} \quad (8)$$

Modeling results are summarized in Figure 13A,B along with a graphical representation of redox cycling across a redoxcline and hypothetical depth profiles for $[O_{2,\,surface}]$ and $[Fe^{2+}_{deep}]$ (Figure 13C). $[O_{2,\,surface}]$ values that would support a stable redoxcline above the FWWB ($z_{redoxcline} = 10$ m for demonstration purposes) for $[Fe^{2+}_{deep}]$ values from 50 to 500 μM Fe^{2+} (at 50 μM $[Fe^{2+}_{deep}]$ increments) for total model depth of 100 m and 200 m are shown in Table 1. These values are based on previous estimates for $[Fe^{2+}_{(aq)}]$ in IF-forming basins, typically ranging from 10 to 100s of μM Fe^{2+} (Holland 1973; Morris 1993; Thompson et al. 2019). Correspondingly, the necessary pO_2 to maintain these $[O_{2,\,surface}]$ values in the absence of additional, local cyanobacterial O_2 production due to potential Fe toxicity (i.e., O_2 saturation at equilibrium with the atmosphere) is calculated using empirical solubility relationships. According to Henry's Law, the amount of dissolved gas in a liquid is directly proportional to its partial pressure above the fluid. Therefore, calculated pO_2 during deposition of the Gibraltar Formation GIFs as a fraction of the present atmospheric level (PAL) should be directly proportional to the fraction of $[O_{2,\,surface}]$ in surface waters relative to dissolved oxygen in a similar modern aqueous environment ($F_{[O_{2,\,surface}]}$). Herein, pO_2 is calculated using the following equation:

$$pO_2 = F_{[O_{2,\,surface}]} \times 100\% = \frac{[O_{2,\,surface}]}{[O_{2,\,surface}]_{modern}} \times 100\% \quad (9)$$

where $[O_{2,\,surface}]_{modern}$ is dissolved oxygen in mg/L (converted to μM for PAL calculations), in water under the modern oxygenated atmosphere as a function of temperature (T), in°K, calculated using the solubility relationship, and adjusted for salinity (S), in parts per thousand (ppt), with the Setschenow coefficient, F_s, both as defined by Benson and Krause Jr. (1984):

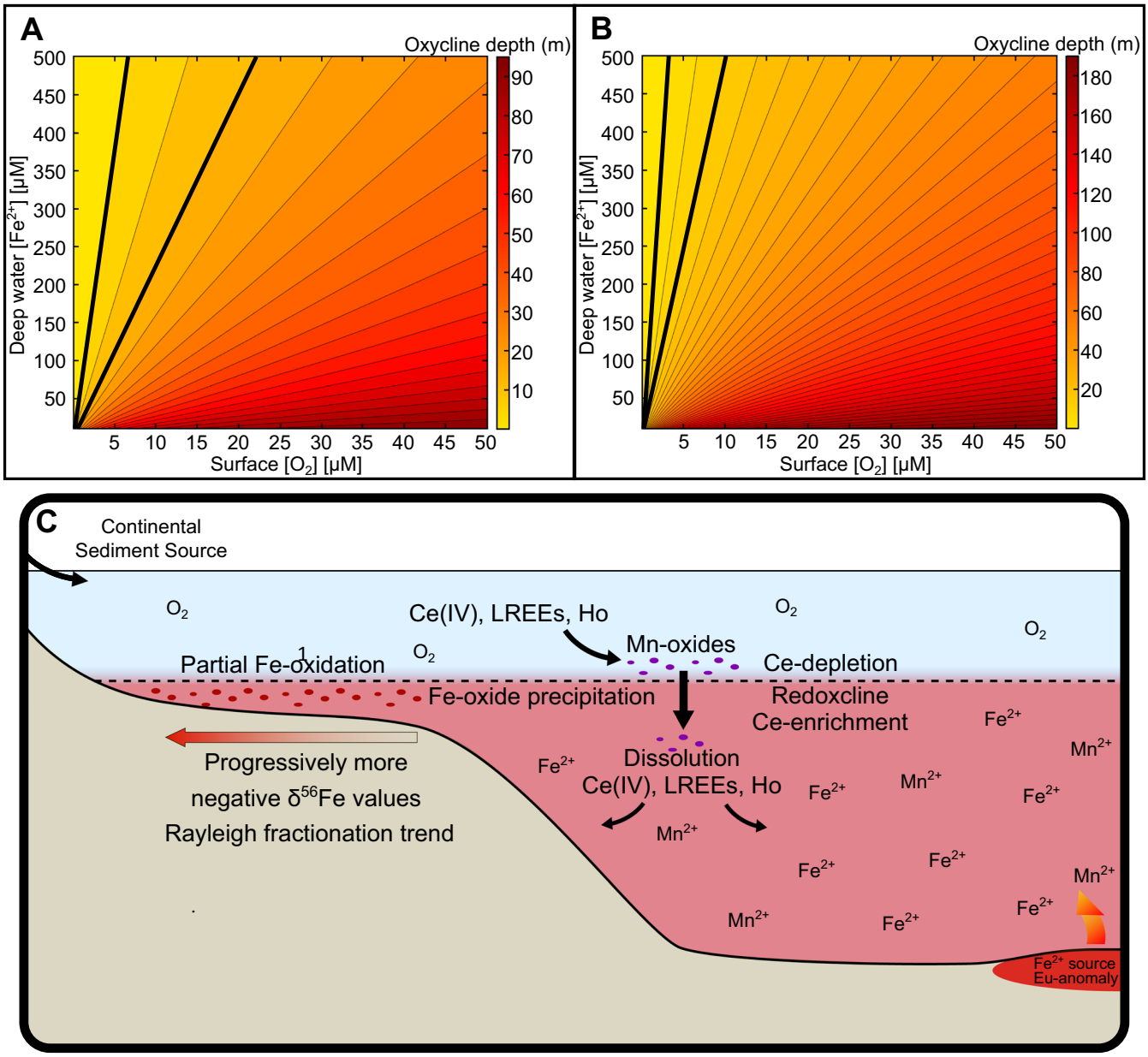

FIGURE 13 | Results of 1D dispersion-reaction modeling. (A and B) Relationship of redoxcline depth as calculated with equation 7 (cf. Heard et al. 2020) with the maximum $[Fe^{2+}]$ in deep waters prior to upwelling and oxidation ($[Fe^{2+}_{deep}]$) and $[O_{2(aq)}]$ above the redoxcline in surface waters in equilibrium with the atmosphere ($[O_{2,\,surface}]$) for continental shelf depth (z_{model}) of 100 and 200 m, respectively. (C) Schematics of redox cycling as anoxic, ferruginous waters upwell into oxygenated waters across a redoxcline. Hydrothermal fluids delivered onto the continental margin would carry a positive Eu anomaly. Ce, LREE, and Ho would preferentially be scavenged by Mn and Fe oxyhydroxides above the redoxcline, resulting in depletion above and enrichment below the redoxcline as suspended particles settled across the redoxcline and redissolved. During partial Fe oxidation in the basin, Fe oxyhydroxides would develop a wide range of $\delta^{56}Fe$ values with a spatial Rayleigh fractionation trend in which $\delta^{56}Fe$ values become progressively more negative with distance from the source.

$$\left[O_{2,\,surface}\right]_{modern} = \exp\left[-139.34411 + \frac{1.575701\times10^{5}}{T} - \frac{6.642308\times10^{7}}{T^{2}} + \frac{1.243800\times10^{10}}{T^{3}} - \frac{8.621949\times10^{11}}{T^{4}}\right]\times F_{s} \quad (10)$$

$$F_s = exp\left[-S\times\left(0.017674 - \frac{10.754}{T} + \frac{2140.7}{T^{2}}\right)\right] \quad (11)$$

Results for atmospheric pO_2 shown in Table 1 were calculated at a T of 25°C (298.15 K) and S of 0.5 and 35 ppt as reference points to modern freshwater and marine systems. To further demonstrate variability, Figure S9 shows the calculated dissolved oxygen under an atmosphere with 0.1%, 1%, and 10% PAL as a function of T ranging from 0°C to 50°C and S of 0.5 and 35 ppt. Considering uncertainties regarding the late Paleoproterozoic atmospheric pressure and climate, we do not apply any corrections to account for atmospheric pressure or wind speed. Further information regarding solubility relationships, variability, and uncertainties can be found in Benson and Krause (1980, 1984), Rounds (2011), and

TABLE 1 | Summarized results of modeling to determine [Fe^{2+}_{deep}] (μM Fe^{2+}) and [$O_{2,\ surface}$] (μM O_2) at a redoxcline depth ($Z_{redoxcline}$) of 10 m and solubility calculations (after Benson and Krause Jr. 1984) for model depths of 100 and 200 m.

[Fe^{2+}_{deep}] (μM)	[$O_{2,\ surface}$] (μM)	%PAL ($S = 0.5$ ppt)	%PAL ($S = 35$ ppt)
$Z_{model} = 100$			
50.00	1.39	0.54	0.66
100.00	2.78	1.08	1.31
150.00	4.17	1.62	1.97
200.00	5.56	2.16	2.63
250.00	6.94	2.70	3.28
300.00	8.33	3.24	3.94
350.00	9.72	3.78	4.59
400.00	11.11	4.31	5.25
450.00	12.50	4.85	5.91
500.00	13.89	5.39	6.56
$Z_{model} = 200$			
50.00	0.66	0.26	0.31
100.00	1.32	0.51	0.62
150.00	1.97	0.77	0.93
200.00	2.63	1.02	1.24
250.00	3.29	1.28	1.55
300.00	3.95	1.53	1.87
350.00	4.61	1.79	2.18
400.00	5.26	2.04	2.49
450.00	5.92	2.30	2.80
500.00	6.58	2.55	3.11

Sander (2023). Although aqueous O_2 saturation is complicated by numerous factors, waters in shallow, coastal marine environments affected by wave activity regularly reach saturation or supersaturation with respect to atmospheric O_2 (Giomi et al. 2023). Aqueous O_2 saturation is therefore a useful reference. For another example, which employed different methods that also account for wind speed, see Wang et al. (2022).

For the ca. 500 Myr before the widespread deposition of ca. 1.88 Ga GIFs, IF deposition was limited by a combination of tectonomagmatic and environmental controls, including an increase in pO_2 during the GOE (Bekker and Holland 2012). However, a significant decrease in global primary organic productivity at the end of the GOE, inferred from a negative shift in triple oxygen isotope values of marine sulfate evaporites in the Belcher Group, associated with recovery from the oxygen overshoot, is consistent with a transition to lower pO_2 levels in the aftermath of the GOE (Crockford et al. 2019; Hodgskiss et al. 2019). While some recent estimates based on Se/Co in sedimentary pyrites argue for high atmospheric pO_2 in the late Paleoproterozoic, ranging from ~48% to 119% PAL (~10 to 25 wt.%; Large et al. 2019; Steadman et al. 2020), most studies support a much lower atmospheric pO_2. Constraining the inferred lower limit, the chromium isotope composition of late Paleoproterozoic paleosols and IFs has been used to argue for atmospheric pO_2 <1.0% PAL (e.g., Planavsky et al. 2014; Colwyn et al. 2019). The latter pO_2 estimate for the late Paleoproterozoic is further supported by the absence of large Ce anomalies in the late Paleoproterozoic Pethei Group carbonates (Bellefroid et al. 2018).

Most plausible estimates of the atmospheric oxygen during the late Paleoproterozoic, in the range of <1 to 10% PAL (Canfield 1998; Rye and Holland 1998; Lyons, Reinhard, and Planavsky 2014; Planavsky et al. 2014; Bellefroid et al. 2018; Daines et al. 2017; Colwyn et al. 2019), would result in a water column [$O_{2(aq)}$] range of 0.27–27 μM O_2. The above calculations highlight that atmospheric pO_2 between ~0.1% and 7% PAL is sufficient to maintain the redoxcline at or above the FWWB. Higher estimates (cf. Large et al. 2019; Steadman et al. 2020) would have hindered the widespread development of ferruginous environments in shallow-water settings above the FWWB. It is important to emphasize that these calculations represent maximum estimates. Factors such as local cyanobacterial O_2 production or an even shallower position of the redoxcline would result in lower values for pO_2.

This short-term, widespread proliferation of FeOB microbial communities in shallow-marine, basinal settings in Earth's history seems to have been enabled not only by a transient, large-scale Fe supply from increased submarine volcanism but also by a higher atmospheric pO_2 than was present when pre-GOE BIFs were deposited, which helped establish the necessary and yet widespread redox-stratified environments. Calculations herein highlight that an upper estimate of atmospheric pO_2, which would support widespread, thriving FeOB communities during episodes of stifled local cyanobacterial O_2 production due to Fe toxicity, lies in the range of ~0.1%–7.0% PAL. In modern ferruginous environments, Fe oxidation by FeOB typically outcompetes abiotic $Fe^{2+}_{(aq)}$ oxidation at [$O_{2(aq)}$] below 50 μM O_2 (Druschel et al. 2008; McAllister et al. 2019). FeOB at the Kama'ehuakanaloa Seamount thrive in low-temperature, hydrothermal settings where bottom-water [$O_{2(aq)}$] is ~30 μM O_2 (Glazer and Rouxel 2009). Laboratory culture experiments have shown that optimal conditions for some FeOB lie in the range of 5–20 μM [O_2] (Maisch et al. 2019), overlapping with the [$O_{2,\ surface}$] values calculated herein. Although FeOB continue to oxidize $Fe^{2+}_{(aq)}$ at sub-μM [O_2] (Chiu et al. 2017; McAllister et al. 2019), our calculations demonstrate that pO_2 in the late Paleoproterozoic being higher than before, but lower than during the GOE, primed shallow-water, shoreface settings at and above the FWWB with sufficient [$O_{2(aq)}$] for the proliferation of FeOB microbial communities at times when local O_2 production by cyanobacteria was stifled by Fe toxicity below and at the redoxcline.

Although the results of these calculations constitute a relatively large range for atmospheric oxygen, they are consistent with lower estimates for the late Paleoproterozoic. In contrast to modern, oxygenated Earth's surface conditions, where FeOB are restricted by $Fe^{2+}_{(aq)}$ availability to environments near its sources, in the Fe^{2+}-rich oceans before the GOE, these organisms may have instead been limited by dissolved O_2 availability.

Ca. 1.88 Ga GIF deposition may, therefore, represent a temporally restricted, but spatially widespread episode of optimal biogeochemical conditions in Earth's history when FeOB metabolic $Fe^{2+}_{(aq)}$ and $O_{2(aq)}$ requirements were widely accommodated in shallow-marine, depositional settings, resulting in FeOB blooms and GIF deposition.

7 | Conclusions

The ca. 1.89 Ga Gibraltar Formation GIFs provide new paleontological and geochemical insights into late Paleoproterozoic GIF deposition. The results of this study support a widespread proliferation of FeOB at ca. 1.88 Ga, which oxidized $Fe^{2+}_{(aq)}$ in seawater in shallow-marine, shoreface settings to precipitate GIF precursor sediments. Microfossils were found in Fe-rich, stromatolitic facies of the Gibraltar Formation, some of which show a twisted filamentous morphology and, rarely, a rounded structure attached at one end, bearing resemblance to the modern, stalk-forming FeOB Zetaproteobacteria *Mariprofundus ferrooxydans*. Major and trace element as well as the REE+Y composition of bulk-rock GIFs are consistent with deposition in a redox-stratified basin. Fe isotope data for bulk-rock and individual stromatolite lamina support direct microbial Fe oxidation by FeOB to form GIFs rather than indirect microbial Fe oxidation by cyanobacterial O_2 production. Small positive Eu anomalies, moderately negative to slightly positive ε_{Nd}(1.89 Ga) values, Fe isotope values at or above that of hydrothermal vent fluids, and basinal geochemical trends suggest a significant hydrothermal Fe source to the basin, likely linked to a mantle plume event that enhanced submarine volcanism. Broadly, these findings confirm that the prevalence of FeOB at ca. 1.88 Ga in GIF-depositing basins was paleogeographically widespread.

Under the assumption that cyanobacteria may have been inhibited by Fe toxicity under ferruginous conditions at and below the redoxcline, we explore the balance between $[Fe^{2+}_{(aq)}]$ in upwelling deep waters and $[O_{2(aq)}]$ in shallow waters aerated via atmospheric diffusion, which would situate a redoxcline at or above the FWWB (around 10 m or shallower). We determine the atmospheric pO_2 that would support such a shallow-water redoxcline. Optimal conditions for Fe oxidation by shallow-marine FeOB communities could have been met at atmospheric pO_2 of ~0.1%–7% PAL, consistent with most previous estimates for the late Paleoproterozoic. Any local oxygen production by cyanobacteria that escaped Fe toxicity would allow for lower values, so the inferred range can be considered potentially maximum values.

Nonetheless, these calculations underscore the crucial impact of the redox landscape on the late Paleoproterozoic biosphere. In contrast to modern, well-oxygenated atmospheric conditions, where FeOB are restricted to environments near $Fe^{2+}_{(aq)}$ sources, or the far more reducing pre-GOE atmosphere, where FeOB would have been limited to environments with sufficient O_2 availability, this ca. 1.88 Ga GIF-depositing episode highlights a restricted time interval in Earth's history. During this unique, relatively short period, $Fe^{2+}_{(aq)}$—$O_{2(aq)}$ gradients suitable for FeOB metabolic needs were widely developed in shallow-marine, shoreface environments at and above the FWWB. We interpret the widespread GIF deposition at ca. 1.88 Ga as a distinctive, temporally restricted episode of optimal biogeochemical conditions for FeOB in Earth's history, when a balance between increased hydrothermal Fe flux from the deep oceans and a moderate, late Paleoproterozoic atmospheric pO_2 globally accommodated FeOB metabolic $Fe^{2+}_{(aq)}$ and $O_{2(aq)}$ requirements in shallow-marine, shoreface environments.

Acknowledgments

We thank Sergio Padilla Ramirez for analytical support of Sm-Nd isotope analyses at CICESE. Funding to Alex Kovalick was provided by the Society of Economic Geologists—Graduate Student Fellowship Program. Fieldwork (LO, AB) was supported by the Northwest Territories Geological Survey and an Aurora Research Institute NWT Scientific Research License No. 15499 and 15612 (LO). Aircraft access was financially supported by the Polar Continental Shelf Program (LO). Analyses at WHOI were supported financially by a NASA Exobiology grant 80NSSC22K1628 to Andy W. Heard and Sune G. Nielsen. Andy W. Heard was supported by the WHOI Postdoctoral Scholarship program and an Agouron Institute Postdoctoral Fellowship in Geobiology. Funding to Andrey Bekker was provided by the Petroleum Foundation of the American Chemical Society grant 624840ND2 and the NSERC Discovery and Accelerator Grants. Funding for Aleisha C. Johnson was provided by the National Science Foundation Earth Sciences Postdoctoral Fellowships (EAR-PF) (1952809). CONACyT provided support for the Nu Instruments TIMS via infrastructure grant INFR-2016-01-269082.

Conflicts of Interest

The authors declare no conflicts of interest.

Data Availability Statement

The data that supports the findings of this study are available in the supplementary material of this article.

References

Alexander, B. W., M. Bau, P. Andersson, and P. Dulski. 2008. "Continentally-Derived Solutes in Shallow Archean Seawater: Rare Earth Element and Nd Isotope Evidence in Iron Formation From the 2.9Ga Pongola Supergroup." *South Africa. Geochimica et Cosmochimica Acta* 72: 378–394. https://doi.org/10.1016/j.gca.2007.10.028.

Alibo, D. S., and Y. Nozaki. 1999. "Rare Earth Elements in Seawater: Particle Association, Shale-Normalization, and Ce Oxidation." *Geochimica et Cosmochimica Acta* 63: 363–372.

Awramik, S. M., and E. S. Barghoorn. 1977. "The Gunflint Microbiota." *Precambrian Research* 5: 121–142. https://doi.org/10.1016/0301-9268(77)90025-0.

Babechuk, M. G., I. C. Kleinhanns, and R. Schoenberg. 2017. "Chromium Geochemistry of the ca. 1.85 Ga Flin Flon Paleosol." *Geobiology* 15: 30–50. https://doi.org/10.1111/gbi.12203.

Baker, I. R., S. L. Matzen, C. J. Schuler, B. M. Toner, and P. R. Girguis. 2023. "Aerobic Iron-Oxidizing Bacteria Secrete Metabolites That Markedly Impede Abiotic Iron Oxidation." *PNAS Nexus* 2: pgad421. https://doi.org/10.1093/pnasnexus/pgad421.

Balci, N., T. D. Bullen, K. Witte-Lien, W. C. Shanks, M. Motelica, and K. W. Mandernack. 2006. "Iron Isotope Fractionation During Microbially Stimulated Fe(II) Oxidation and Fe(III) Precipitation." *Geochimica et Cosmochimica Acta* 70: 622–639. https://doi.org/10.1016/j.gca.2005.09.025.

Barghoorn, E. S., and S. A. Tyler. 1965. "Microorganisms From the Gunflint Chert." *Science* 147: 563–575. https://doi.org/10.1126/science.147.3658.563.

Barley, M. E., A. Bekker, and B. Krapež. 2005. "Late Archean to Early Paleoproterozoic Global Tectonics, Environmental Change and the Rise of Atmospheric Oxygen." *Earth and Planetary Science Letters* 238: 156–171. https://doi.org/10.1016/j.epsl.2005.06.062.

Bau, M. 1999. "Scavenging of Dissolved Yttrium and Rare Earths by Precipitating Iron Oxyhydroxide: Experimental Evidence for Ce Oxidation, Y-Ho Fractionation, and Lanthanide Tetrad Effect." *Geochimica et Cosmochimica Acta* 63: 67–77. https://doi.org/10.1016/S0016-7037(99)00014-9.

Bau, M., and P. Dulski. 1996. "Distribution of Yttrium and Rare-Earth Elements in the Penge and Kuruman Iron-Formations, Transvaal Supergroup, South Africa." *Precambrian Research* 79: 37–55. https://doi.org/10.1016/0301-9268(95)00087-9.

Bau, M., and A. Koschinsky. 2009. "Oxidative Scavenging of Cerium on Hydrous Fe Oxide: Evidence From the Distribution of Rare Earth Elements and Yttrium Between Fe Oxides and Mn Oxides in Hydrogenetic Ferromanganese Crusts." *Geochemical Journal* 43: 37–47. https://doi.org/10.2343/geochemj.1.0005.

Bau, M., P. Möller, and P. Dulski. 1997. "Yttrium and Lanthanides in Eastern Mediterranean Seawater and Their Fractionation During Redox-Cycling." *Marine Chemistry* 56: 123–131. https://doi.org/10.1016/S0304-4203(96)00091-6.

Bekker, A., and H. D. Holland. 2012. "Oxygen Overshoot and Recovery During the Early Paleoproterozoic." *Earth and Planetary Science Letters* 317–318: 295–304. https://doi.org/10.1016/j.epsl.2011.12.012.

Bekker, A., H. D. Holland, P.-L. Wang, et al. 2004. "Dating the Rise of Atmospheric Oxygen." *Nature* 427: 117–120. https://doi.org/10.1038/nature02260.

Bekker, A., and A. Kovalick. 2021. "Ironstones and Iron Formations." In *Encyclopedia of Geology*, edited by D. Alderton and S. A. Elias, 2nd ed., 914–921. Oxford: Academic Press. https://doi.org/10.1016/B978-0-08-102908-4.00199-5.

Bekker, A., N. J. Planavsky, B. Krapež, et al. 2014. "Iron Formations: Their Origins and Implications for Ancient Seawater Chemistry." In *Treatise on Geochemistry*, 561–628. Oxford: Elsevier. https://doi.org/10.1016/B978-0-08-095975-7.00719-1.

Bellefroid, E. J., A. V. S. Hood, P. F. Hoffman, M. D. Thomas, C. T. Reinhard, and N. J. Planavsky. 2018. "Constraints on Paleoproterozoic Atmospheric Oxygen Levels." *Proceedings of the National Academy of Sciences* 115: 8104–8109. https://doi.org/10.1073/pnas.1806216115.

Bellefroid, E. J., N. J. Planavsky, A. V. S. Hood, G. P. Halverson, and K. Spokas. 2019. "Shallow Water Redox Conditions of the Mid-Proterozoic Muskwa Assemblage, British Columbia, Canada." *American Journal of Science* 319: 122–157. https://doi.org/10.2475/02.2019.03.

Bennett, S. A., B. M. Toner, R. Barco, and K. J. Edwards. 2014. "Carbon Adsorption Onto Fe Oxyhydroxide Stalks Produced by a Lithotrophic Iron-Oxidizing Bacteria." *Geobiology* 12: 146–156. https://doi.org/10.1111/gbi.12074.

Benson, B. B., and D. Krause Jr. 1980. "The Concentration and Isotopic Fractionation of Gases Dissolved in Freshwater in Equilibrium With the Atmosphere. 1." *Oxygen. Limnology and Oceanography* 25: 662–671. https://doi.org/10.4319/lo.1980.25.4.0662.

Benson, B. B., and D. Krause Jr. 1984. "The Concentration and Isotopic Fractionation of Oxygen Dissolved in Freshwater and Seawater in Equilibrium With the Atmosphere1." *Limnology and Oceanography* 29: 620–632. https://doi.org/10.4319/lo.1984.29.3.0620.

Berman, R. G., J. A. Cutts, W. J. Davis, A. Camacho, M. Sanborn-Barrie, and M. A. Smit. 2023. "The Tectonic Evolution of Thelon Tectonic Zone, Canada: A New Model Based on Petrological Modeling Linked With Lu–Hf Garnet and U–Pb Accessory Mineral Geochronology." *Canadian Journal of Earth Sciences* 60: 550–582. https://doi.org/10.1139/cjes-2022-0147.

Bouvier, A., J. D. Vervoort, and P. J. Patchett. 2008. "The Lu–Hf and Sm–Nd Isotopic Composition of CHUR: Constraints From Unequilibrated Chondrites and Implications for the Bulk Composition of Terrestrial Planets." *Earth and Planetary Science Letters* 273: 48–57. https://doi.org/10.1016/j.epsl.2008.06.010.

Bowring, S. A., and J. P. Grotzinger. 1992. "Implications of New Chronostratigraphy for Tectonic Evolution of Wopmay Orogen, Northwest Canadian Shield." *American Journal of Science* 292: 1–20.

Bowring, S. A., W. R. V. Schmus, and P. F. Hoffman. 1984. "U–Pb Zircon Ages From Athapuscow Aulacogen, East Arm of Great Slave Lake, N.W.T., Canada." *Canadian Journal of Earth Sciences* 21: 1315–1324. https://doi.org/10.1139/e84-136.

Buchan, K. L., R. N. Mitchell, W. Bleeker, M. A. Hamilton, and A. N. LeCheminant. 2016. "Paleomagnetism of Ca. 2.13–2.11 Ga Indin and Ca. 1.885 Ga Ghost Dyke Swarms of the Slave Craton: Implications for the Slave Craton APW Path and Relative Drift of Slave, Superior and Siberian Cratons in the Paleoproterozoic." *Precambrian Research* 275: 151–175. https://doi.org/10.1016/j.precamres.2016.01.012.

Bullen, T. D., A. F. White, C. W. Childs, D. V. Vivit, and M. S. Schulz. 2001. "Demonstration of Significant Abiotic Iron Isotope Fractionation in Nature." *Geology* 29: 699. https://doi.org/10.1130/0091-7613(2001)029<0699:DOSAII>2.0.CO;2.

Byrne, R. H., and E. R. Sholkovitz. 1996. "Chapter 158 Marine Chemistry and Geochemistry of the Lanthanides." In *Handbook on the Physics and Chemistry of Rare Earths*, 497–593. Amsterdam: Elsevier. https://doi.org/10.1016/S0168-1273(96)23009-0.

Canfield, D. E. 1998. "A New Model for Proterozoic Ocean Chemistry." *Nature* 396: 450–453. https://doi.org/10.1038/24839.

Canfield, D. E., and B. Thamdrup. 2009. "Towards a Consistent Classification Scheme for Geochemical Environments, or, Why We Wish the Term 'Suboxic' Would Go Away." *Geobiology* 7: 385–392. https://doi.org/10.1111/j.1472-4669.2009.00214.x.

Castenholz, R. W. 1969. "Thermophilic Blue-Green Algae and the Thermal Environment." *Bacteriological Reviews* 33: 476–504. https://doi.org/10.1128/br.33.4.476-504.1969.

Chan, C. S., D. Emerson, and G. W. Luther. 2016. "The Role of Microaerophilic Fe-Oxidizing Micro-Organisms in Producing Banded Iron Formations." *Geobiology* 14: 509–528. https://doi.org/10.1111/gbi.12192.

Chan, C. S., S. C. Fakra, D. Emerson, E. J. Fleming, and K. J. Edwards. 2011. "Lithotrophic Iron-Oxidizing Bacteria Produce Organic Stalks to Control Mineral Growth: Implications for Biosignature Formation." *ISME Journal* 5: 717–727. https://doi.org/10.1038/ismej.2010.173.

Chan, C. S., S. M. McAllister, A. H. Leavitt, B. T. Glazer, S. T. Krepski, and D. Emerson. 2016. "The Architecture of Iron Microbial Mats Reflects the Adaptation of Chemolithotrophic Iron Oxidation in Freshwater and Marine Environments." *Frontiers in Microbiology* 7: 796. https://doi.org/10.3389/fmicb.2016.00796.

Chen, J., T. J. Algeo, L. Zhao, et al. 2015. "Diagenetic Uptake of Rare Earth Elements by Bioapatite, With an Example From Lower Triassic Conodonts of South China." *Earth-Science Reviews* 149: 181–202. https://doi.org/10.1016/j.earscirev.2015.01.013.

Chiu, B. K., S. Kato, S. M. McAllister, E. K. Field, and C. S. Chan. 2017. "Novel Pelagic Iron-Oxidizing Zetaproteobacteria From the Chesapeake Bay Oxic–Anoxic Transition Zone." *Frontiers in Microbiology* 8: 1280.

Cloud, P. E. 1965. "Significance of the Gunflint (Precambrian) Microflora: Photosynthetic Oxygen May Have Had Important Local Effects Before Becoming a Major Atmospheric Gas." *Science* 148: 27–35. https://doi.org/10.1126/science.148.3666.27.

Colwyn, D. A., N. D. Sheldon, J. B. Maynard, et al. 2019. "A Paleosol Record of the Evolution of Cr Redox Cycling and Evidence for an

Increase in Atmospheric Oxygen During the Neoproterozoic." *Geobiology* 17: 579–593. https://doi.org/10.1111/gbi.12360.

Condie, K. C. 1993. "Chemical Composition and Evolution of the Upper Continental Crust: Contrasting Results From Surface Samples and Shales." *Chemical Geology* 104: 1–37. https://doi.org/10.1016/0009-2541(93)90140-E.

Condie, K. C., D. J. Des Marais, and D. Abbott. 2000. "Geologic Evidence for a Mantle Superplume Event at 1.9 Ga: Mantle Superplume Event." *Geochemistry, Geophysics, Geosystems* 1: 1054. https://doi.org/10.1029/2000GC000095.

Croal, L. R., C. M. Johnson, B. L. Beard, and D. K. Newman. 2004. "Iron Isotope Fractionation by Fe(II)-Oxidizing Photoautotrophic Bacteria 11Associate Editor: D." *E. Canfield. Geochimica et Cosmochimica Acta* 68: 1227–1242. https://doi.org/10.1016/j.gca.2003.09.011.

Crockford, P. W., M. Kunzmann, A. Bekker, et al. 2019. "Claypool Continued: Extending the Isotopic Record of Sedimentary Sulfate." *Chemical Geology* 513: 200–225. https://doi.org/10.1016/j.chemgeo.2019.02.030.

Daines, S. J., B. J. W. Mills, and T. M. Lenton. 2017. "Atmospheric Oxygen Regulation at Low Proterozoic Levels by Incomplete Oxidative Weathering of Sedimentary Organic Carbon." *Nature Communications* 8: 14379. https://doi.org/10.1038/ncomms14379.

Dauphas, N., A. W. Heard, E. S. Rego, et al. 2025. "Past and Present Dynamics of the Iron Biogeochemical Cycle." In *Treatise on Geochemistry*, edited by A. Anbar and D. Weis, 3rd ed., 203–244. Oxford: Elsevier. https://doi.org/10.1016/B978-0-323-99762-1.00059-0.

Dauphas, N., A. Pourmand, and F.-Z. Teng. 2009. "Routine Isotopic Analysis of Iron by HR-MC-ICPMS: How Precise and How Accurate?" *Chemical Geology, Advances in Experimental and Theoretical Isotope Geochemistry* 267: 175–184. https://doi.org/10.1016/j.chemgeo.2008.12.011.

De Baar, H. J. W., P. G. Brewer, and M. P. Bacon. 1985. "Anomalies in Rare Earth Distributions in Seawater: Gd and Tb." *Geochimica et Cosmochimica Acta* 49: 1961–1969. https://doi.org/10.1016/0016-7037(85)90090-0.

De Baar, H. J. W., J. Schijf, and R. H. Byrne. 1991. "Solution Chemistry of Rare Earth Elements." *European Journal of Solid State and Inorganic Chemistry* 28: 357–373.

DePaolo, D. J. 1980. "Crustal Growth and Mantle Evolution: Inferences From Models of Element Transport and Nd and Sr Isotopes." *Geochimica et Cosmochimica Acta* 44: 1185–1196. https://doi.org/10.1016/0016-7037(80)90072-1.

Dodd, M. S., D. Papineau, T. Grenne, et al. 2017. "Evidence for Early Life in Earth's Oldest Hydrothermal Vent Precipitates." *Nature* 543: 60–64. https://doi.org/10.1038/nature21377.

Dodd, M. S., D. Papineau, Z. She, M. L. Fogel, S. Nederbragt, and F. Pirajno. 2018. "Organic Remains in Late Palaeoproterozoic Granular Iron Formations and Implications for the Origin of Granules." *Precambrian Research* 310: 133–152. https://doi.org/10.1016/j.precamres.2018.02.016.

Douville, E., P. Bienvenu, J. L. Charlou, et al. 1999. "Yttrium and Rare Earth Elements in Fluids From Various Deep-Sea Hydrothermal Systems." *Geochimica et Cosmochimica Acta* 63: 627–643. https://doi.org/10.1016/S0016-7037(99)00024-1.

Druschel, G. K., D. Emerson, R. Sutka, P. Suchecki, and G. W. Luther III. 2008. "Low-Oxygen and Chemical Kinetic Constraints on the Geochemical Niche of Neutrophilic Iron(II) Oxidizing Microorganisms." *Geochimica et Cosmochimica Acta* 72: 3358–3370. https://doi.org/10.1016/j.gca.2008.04.035.

Emerson, D., and C. L. Moyer. 2002. "Neutrophilic Fe-Oxidizing Bacteria Are Abundant at the Loihi Seamount Hydrothermal Vents and Play a Major Role in Fe Oxide Deposition." *Applied and Environmental Microbiology* 68: 3085–3093. https://doi.org/10.1128/AEM.68.6.3085-3093.2002.

Emerson, D., J. A. Rentz, T. G. Lilburn, et al. 2007. "A Novel Lineage of Proteobacteria Involved in Formation of Marine Fe-Oxidizing Microbial Mat Communities." *PLoS One* 2: e667. https://doi.org/10.1371/journal.pone.0000667.

Eyster, A., L. A. Brengman, C. I. O. Nichols, Z. Levitt, J. Wilcots, and K. D. Bergmann. 2021. "A New Depositional Framework for Massive Iron Formations After the Great Oxidation Event." *Geochemistry, Geophysics, Geosystems* 22: e2020GC009113. https://doi.org/10.1029/2020GC009113.

Findlay, J. M., R. R. Parrish, T. C. Birkett, and D. H. Watanabe. 1995. "U–Pb Ages From the Nimish Formation and Montagnais Glomeroporphyritic Gabbro of the Central New Québec Orogen, Canada." *Canadian Journal of Earth Sciences* 32: 1208–1220. https://doi.org/10.1139/e95-099.

Fralick, P., D. W. Davis, and S. A. Kissin. 2002. "The Age of the Gunflint Formation, Ontario, Canada: Single Zircon UPb Age Determinations From Reworked Volcanic Ash." *Canadian Journal of Earth Sciences* 39: 1085–1091. https://doi.org/10.1139/e02-028.

Frei, R., C. Gaucher, S. W. Poulton, and D. E. Canfield. 2009. "Fluctuations in Precambrian Atmospheric Oxygenation Recorded by Chromium Isotopes." *Nature* 461: 250–253. https://doi.org/10.1038/nature08266.

Gao, S., and K. H. Wedepohl. 1995. "The Negative Eu Anomaly in Archean Sedimentary Rocks: Implications for Decomposition, Age and Importance of Their Granitic Sources." *Earth and Planetary Science Letters* 133: 81–94. https://doi.org/10.1016/0012-821X(95)00077-P.

German, C. R., B. P. Holliday, and H. Elderfield. 1991. "Redox Cycling of Rare Earth Elements in the Suboxic Zone of the Black Sea." *Geochimica et Cosmochimica Acta* 55: 3553–3558. https://doi.org/10.1016/0016-7037(91)90055-A.

Giomi, F., A. Barausse, A. Steckbauer, D. Daffonchio, C. M. Duarte, and M. Fusi. 2023. "Oxygen Dynamics in Marine Productive Ecosystems at Ecologically Relevant Scales." *Nature Geoscience* 16: 560–566. https://doi.org/10.1038/s41561-023-01217-z.

Glazer, B. T., and O. J. Rouxel. 2009. "Redox Speciation and Distribution Within Diverse Iron-Dominated Microbial Habitats at Loihi Seamount." *Geomicrobiology Journal* 26: 606–622. https://doi.org/10.1080/01490450903263392.

Gong, Y., Y. Xia, F. Huang, and H. Yu. 2017. "Average Iron Isotopic Compositions of the Upper Continental Crust: Constrained by Loess From the Chinese Loess Plateau." *Acta Geochimica* 36: 125–131. https://doi.org/10.1007/s11631-016-0131-5.

Greber, N. D., N. Dauphas, A. Bekker, M. P. Ptáček, I. N. Bindeman, and A. Hofmann. 2017. "Titanium Isotopic Evidence for Felsic Crust and Plate Tectonics 3.5 Billion Years Ago." *Science* 357: 1271–1274. https://doi.org/10.1126/science.aan8086.

Gumsley, A. P., K. R. Chamberlain, W. Bleeker, et al. 2017. "Timing and Tempo of the Great Oxidation Event." *Proceedings of the National Academy of Sciences* 114: 1811–1816. https://doi.org/10.1073/pnas.1608824114.

Haley, B. A., G. P. Klinkhammer, and J. McManus. 2004. "Rare Earth Elements in Pore Waters of Marine Sediments." *Geochimica et Cosmochimica Acta* 68: 1265–1279. https://doi.org/10.1016/j.gca.2003.09.012.

Hannigan, R. E., and E. R. Sholkovitz. 2001. "The Development of Middle Rare Earth Element Enrichments in Freshwaters: Weathering of Phosphate Minerals." *Chemical Geology* 175: 495–508. https://doi.org/10.1016/S0009-2541(00)00355-7.

Haugaard, R., L. Ootes, R. A. Creaser, and K. O. Konhauser. 2016. "The Nature of Mesoarchaean Seawater and Continental Weathering in 2.85Ga Banded Iron Formation, Slave Craton." *NW Canada.*

Geochimica et Cosmochimica Acta 194: 34–56. https://doi.org/10.1016/j.gca.2016.08.020.

Heard, A. W., A. Bekker, A. Kovalick, H. Tsikos, T. Ireland, and N. Dauphas. 2022. "Oxygen Production and Rapid Iron Oxidation in Stromatolites Immediately Predating the Great Oxidation Event." *Earth and Planetary Science Letters* 582: 117416. https://doi.org/10.1016/j.epsl.2022.117416.

Heard, A. W., N. Dauphas, R. Guilbaud, et al. 2020. "Triple Iron Isotope Constraints on the Role of Ocean Iron Sinks in Early Atmospheric Oxygenation." *Science* 370: 446–449. https://doi.org/10.1126/science.aaz8821.

Hiebert, R. S., A. Bekker, M. G. Houlé, and O. J. Rouxel. 2018. "Depositional Setting of the Late Archean Fe Oxide- and Sulfide-Bearing Chert and Graphitic Argillite in the Shaw Dome, Abitibi Greenstone Belt, Canada." *Precambrian Research* 311: 98–116. https://doi.org/10.1016/j.precamres.2018.04.004.

Hildebrand, R. S., P. F. Hoffman, and S. A. Bowring. 2010. "The Calderian Orogeny in Wopmay Orogen (1.9 Ga), northwestern Canadian Shield." *GSA Bulletin* 122: 794–814. https://doi.org/10.1130/B26521.1.

Hirst, C., P. S. Andersson, E. Kooijman, et al. 2020. "Iron Isotopes Reveal the Sources of Fe-Bearing Particles and Colloids in the Lena River Basin." *Geochimica et Cosmochimica Acta* 269: 678–692. https://doi.org/10.1016/j.gca.2019.11.004.

Hodgskiss, M. S. W., P. W. Crockford, Y. Peng, B. A. Wing, and T. J. Horner. 2019. "A Productivity Collapse to End Earth's Great Oxidation." *Proceedings of the National Academy of Sciences* 116: 17207–17212. https://doi.org/10.1073/pnas.1900325116.

Hodgskiss, M. S. W., S. V. Lalonde, P. W. Crockford, and A. M. Hutchings. 2021. "A Carbonate Molybdenum Isotope and Cerium Anomaly Record Across the End-GOE: Local Records of Global Oxygenation." *Geochimica et Cosmochimica Acta* 313: 313–339. https://doi.org/10.1016/j.gca.2021.08.013.

Hoffman, P. 1973. "Evolution of an Early Proterozoic Continental Margin: The Coronation Geosyncline and Associated Aulacogens of the Northwestern Canadian Shield. Philosophical Transactions of the Royal Society of London." *Series A, Mathematical and Physical Sciences* 273: 547–581.

Hoffman, P. F. 1968. "Stratigraphy of the Lower Proterozoic (Aphebian), Great Slave Supergroup, East Arm of Great Slave Lake, District of Mackenzie (No. 68–42)." https://doi.org/10.4095/100654.

Hoffman, P. F. 1987. "Continental Transform Tectonics: Great Slave Lake Shear Zone (ca. 1.9 Ga), Northwest Canada. Geol 15, 785." https://doi.org/10.1130/0091-7613(1987)15<785:CTTGSL>2.0.CO;2.

Hoffman, P. F. 1988a. "Geology and Tectonics, East Arm of Great Slave Lake, Northwest Territories." Geological Survey of Canada, Map 1628A (2 sheets), Scales 1:250,000 (Geology) and 1:500,000 (Tectonics).

Hoffman, P. F. 1988b. "United Plates of America, the Birth of a Craton: Early Proterozoic Assembly and Growth of Laurentia." *Annual Review of Earth and Planetary Sciences* 16: 543–603. https://doi.org/10.1146/annurev.ea.16.050188.002551.

Hoffman, P. F., D. S. Abbot, Y. Ashkenazy, et al. 2017. "Snowball Earth Climate Dynamics and Cryogenian Geology-Geobiology." *Science Advances* 3: e1600983. https://doi.org/10.1126/sciadv.1600983.

Hoffman, P. F., J. F. Dewey, K. Burke. 1974. "Aulacogens and Their Genetic Relation to Geosynclines, With a Proterozoic Example from Great Slave Lake, Canada." In *Modern and Ancient Geosynclinal Sedimentation*, edited by R. H. Dott Jr., and R. H. Shaver, 38–55: Society of Economic Paleontologists and Mineralogists, Special Publication. https://doi.org/10.2110/pec.74.19.0038.

Hoffman, P. F., S. A. Bowring, R. Buchwaldt, and R. S. Hildebrand. 2011. "Birthdate for the Coronation Paleocean: Age of Initial Rifting in Wopmay Orogen, Canada This Article Is One of a Series of Papers Published in This Special Issue on the Theme of Geochronology in Honour of Tom Krogh." *Canadian Journal of Earth Sciences* 48: 281–293. https://doi.org/10.1139/E10-038.

Hoffman, P. F., F. A. Macdonald, S. A. Bowring, et al. 2023. "Crustal Eduction and Slab-Failure Magmatism in an Orosirian (2.05–1.80 Ga) Postcollisional Cratonic Foredeep: Geochronology of Seton Volcanics and Compton Laccoliths, Tu Cho (Great Slave Lake), NWT, Canada." *Canadian Journal of Earth Sciences* 60: 1359–1384. https://doi.org/10.1139/cjes-2023-0011.

Holland, H. D. 1973. "The Oceans; A Possible Source of Iron in Iron-Formations." *Economic Geology* 68: 1169–1172. https://doi.org/10.2113/gsecongeo.68.7.1169.

Holland, H. D. 2002. "Volcanic Gases, Black Smokers, and the Great Oxidation Event." *Geochimica et Cosmochimica Acta* 66: 3811–3826. https://doi.org/10.1016/S0016-7037(02)00950-X.

Hu, J., H. Wang, and L. Zhang. 2020. "A Rare Earth Element and Nd Isotopic Investigation Into the Provenance and Deposition of the Dahongliutan Banded Iron Formation and Associated Carbonates, NW China: Implications on Neoproterozoic Seawater Compositions." *Precambrian Research* 342: 105685. https://doi.org/10.1016/j.precamres.2020.105685.

Isley, A. E., and D. H. Abbott. 1999. "Plume-Related Mafic Volcanism and the Deposition of Banded Iron Formation." *Journal of Geophysical Research: Solid Earth* 104: 15461–15477. https://doi.org/10.1029/1999JB900066.

Jackson, V. A., O. van Breemen, L. Ootes, et al. 2013. "U–Pb Zircon Ages and Field Relationships of Archean Basement and Proterozoic Intrusions, South-Central Wopmay Orogen, NWT: Implications for Tectonic assignments1,2." *Canadian Journal of Earth Sciences* 50: 979–1006. https://doi.org/10.1139/cjes-2013-0046.

Jacobsen, S. B., and M. R. Pimentel-Klose. 1988. "A Nd Isotopic Study of the Hamersley and Michipicoten Banded Iron Formations: The Source of REE and Fe in Archean Oceans." *Earth and Planetary Science Letters* 87: 29–44.

James, H. L. 1954. "Sedimentary Facies of Iron-Formation." *Economic Geology* 49: 235–293. https://doi.org/10.2113/gsecongeo.49.3.235.

Johnson, B. J. 1990. "Stratigraphy and Structure of the Early Proterozoic Wilson Island Group, East Arm Thrust-Fold Belt, N.W.T." *Canadian Journal of Earth Sciences* 27: 552–569. https://doi.org/10.1139/e90-052.

Johnson, C., B. Beard, and S. Weyer. 2020. *Iron Geochemistry: An Isotopic Perspective, Advances in Isotope Geochemistry*. Cham: Springer International Publishing. https://doi.org/10.1007/978-3-030-33828-2.

Johnson, D. B., M.-A. Dziurla, A. Kolmert, and K. B. Hallberg. 2002. "The Microbiology of Acid Mine Drainage: Genesis and Biotreatment: Review Article." *South African Journal of Science* 98: 249–255. https://doi.org/10.10520/EJC97484.

Kappler, A., C. M. Johnson, H. A. Crosby, B. L. Beard, and D. K. Newman. 2010. "Evidence for Equilibrium Iron Isotope Fractionation by Nitrate-Reducing Iron(II)-oxidizing bacteria." *Geochimica et Cosmochimica Acta* 74: 2826–2842. https://doi.org/10.1016/j.gca.2010.02.017.

Khan, R. M. K., S. Das Sharma, D. J. Patil, and S. M. Naqvi. 1996. "Trace, Rare-Earth Element, and Oxygen Isotopic Systematics for the Genesis of Banded Iron-Formations: Evidence From Kushtagi Schist Belt, Archaean Dharwar Craton, India." *Geochimica et Cosmochimica Acta* 60: 3285–3294. https://doi.org/10.1016/0016-7037(96)00172-X.

Kiyokawa, S., T. Kuratomi, T. Hoshino, S. Goto, and M. Ikehara. 2021. "Hydrothermal Formation of Iron-Oxyhydroxide Chimney Mounds in a Shallow Semi-Enclosed Bay at Satsuma Iwo-Jima Island, Kagoshima, Japan." *GSA Bulletin* 133: 1890–1908. https://doi.org/10.1130/B35782.1.

Knoll, A. H., and B. Simonson. 1981. "Early Proterozoic Microfossils and Penecontemporaneous Quartz Cementation in the Sokoman Iron Formation, Canada." *Science* 211: 478–480. https://doi.org/10.1126/science.211.4481.478.

Köhler, I., K. O. Konhauser, D. Papineau, A. Bekker, and A. Kappler. 2013. "Biological Carbon Precursor to Diagenetic Siderite With Spherical Structures in Iron Formations." *Nature Communications* 4: 1741. https://doi.org/10.1038/ncomms2770.

Konhauser, K. O., N. J. Planavsky, D. S. Hardisty, et al. 2017. "Iron Formations: A Global Record of Neoarchaean to Palaeoproterozoic Environmental History." *Earth-Science Reviews* 172: 140–177. https://doi.org/10.1016/j.earscirev.2017.06.012.

Krepski, S. T., T. E. Hanson, and C. S. Chan. 2012. "Isolation and Characterization of a Novel Biomineral Stalk-Forming Iron-Oxidizing Bacterium From a Circumneutral Groundwater Seep." *Environmental Microbiology* 14: 1671–1680. https://doi.org/10.1111/j.1462-2920.2011.02652.x.

Kulaksız, S., and M. Bau. 2011. "Rare Earth Elements in the Rhine River, Germany: First Case of Anthropogenic Lanthanum as a Dissolved Microcontaminant in the Hydrosphere." *Environment International* 37: 973–979. https://doi.org/10.1016/j.envint.2011.02.018.

Large, R. R., I. Mukherjee, D. Gregory, J. Steadman, R. Corkrey, and L. V. Danyushevsky. 2019. "Atmosphere Oxygen Cycling Through the Proterozoic and Phanerozoic." *Mineralium Deposita* 54: 485–506. https://doi.org/10.1007/s00126-019-00873-9.

Lawrence, M. G., A. Greig, K. D. Collerson, and B. S. Kamber. 2006. "Rare Earth Element and Yttrium Variability in South East Queensland Waterways." *Aquatic Geochemistry* 12: 39–72. https://doi.org/10.1007/s10498-005-4471-8.

Lechte, M. A., M. W. Wallace, A. Hood, et al. 2019. "Subglacial Meltwater Supported Aerobic Marine Habitats During Snowball Earth." *Proceedings of the National Academy of Sciences* 116: 25478–25483. https://doi.org/10.1073/pnas.1909165116.

Lechte, M. A., M. W. Wallace, A. Hood, and N. Planavsky. 2018. "Cryogenian iron Formations in the Glaciogenic Kingston Peak Formation, California." *Precambrian Research* 310: 443–462. https://doi.org/10.1016/j.precamres.2018.04.003.

Lepp, H., and S. S. Goldich. 1964. "Origin of Precambrian Iron Formations." *Economic Geology* 59: 1025–1060. https://doi.org/10.2113/gsecongeo.59.6.1025.

Li, W., B. L. Beard, and C. M. Johnson. 2015. "Biologically Recycled Continental Iron Is a Major Component in Banded Iron Formations." *Proceedings. National Academy of Sciences. United States of America* 112: 8193–8198. https://doi.org/10.1073/pnas.1505515112.

Little, C. T. S., K. C. Johannessen, S. Bengtson, et al. 2021. "A Late Paleoproterozoic (1.74 Ga) Deep-Sea, Low-Temperature, Iron-Oxidizing Microbial Hydrothermal Vent Community From Arizona, USA." *Geobiology* 19: 228–249. https://doi.org/10.1111/gbi.12434.

Lyons, T. W., C. W. Diamond, N. J. Planavsky, C. T. Reinhard, and C. Li. 2021. "Oxygenation, Life, and the Planetary System During Earth's Middle History: An Overview." *Astrobiology* 21: 906–923. https://doi.org/10.1089/ast.2020.2418.

Lyons, T. W., C. T. Reinhard, and N. J. Planavsky. 2014. "The Rise of Oxygen in Earth's Early Ocean and Atmosphere." *Nature* 506: 307–315. https://doi.org/10.1038/nature13068.

Maisch, M., U. Lueder, K. Laufer, C. Scholze, A. Kappler, and C. Schmidt. 2019. "Contribution of Microaerophilic Iron(II)-Oxidizers to Iron(III) Mineral Formation." *Environmental Science & Technology* 53: 8197–8204. https://doi.org/10.1021/acs.est.9b01531.

McAllister, S. M., R. M. Moore, A. Gartman, G. W. Luther, D. Emerson, and C. S. Chan. 2019. "The Fe(II)-Oxidizing *Zetaproteobacteria*: Historical, Ecological and Genomic Perspectives." *FEMS Microbiology Ecology* 95: 1–18. https://doi.org/10.1093/femsec/fiz015.

McCulloch, M. T., R. T. Gregory, G. J. Wasserburg, and H. P. Taylor Jr. 1981. "Sm-Nd, Rb-Sr, and 18O/16O Isotopic Systematics in an Oceanic Crustal Section: Evidence From the Samail Ophiolite." *Journal of Geophysical Research: Solid Earth* 86: 2721–2735. https://doi.org/10.1029/JB086iB04p02721.

Michard, A., G. Michard, D. Stüben, P. Stoffers, J.-L. Cheminée, and N. Binard. 1993. "Submarine Thermal Springs Associated With Young Volcanoes: The Teahitia Vents, Society Islands, Pacific Ocean." *Geochimica et Cosmochimica Acta* 57: 4977–4986. https://doi.org/10.1016/S0016-7037(05)80003-1.

Miller, R. G., and R. K. O'Nions. 1985. "Source of Precambrian Chemical and Clastic Sediments." *Nature* 314: 325–330. https://doi.org/10.1038/314325a0.

Moffett, J. W. 1994. "The Relationship Between Cerium and Manganese Oxidation in the Marine Environment." *Limnology and Oceanography* 39: 1309–1318. https://doi.org/10.4319/lo.1994.39.6.1309.

Morris, R. C. 1993. "Genetic Modelling for Banded Iron-Formation of the Hamersley Group, Pilbara Craton, Western Australia." *Precambrian Research* 60: 243–286. https://doi.org/10.1016/0301-9268(93)90051-3.

Mulholland, D. S., F. Poitrasson, L. S. Shirokova, et al. 2015. "Iron Isotope Fractionation During Fe(II) and Fe(III) Adsorption on Cyanobacteria." *Chemical Geology* 400: 24–33. https://doi.org/10.1016/j.chemgeo.2015.01.017.

Nie, N. X., N. Dauphas, and R. C. Greenwood. 2017. "Iron and Oxygen Isotope Fractionation During Iron UV Photo-Oxidation: Implications for Early Earth and Mars." *Earth and Planetary Science Letters* 458: 179–191. https://doi.org/10.1016/j.epsl.2016.10.035.

Nie, N. X., N. Dauphas, K. L. Villalon, et al. 2020. "Iron Isotopic and Chemical Tracing of Basalt Alteration and Hematite Spherule Formation in Hawaii: A Prospective Study for Mars." *Earth and Planetary Science Letters* 544: 116385. https://doi.org/10.1016/j.epsl.2020.116385.

Nozaki, Y., J. Zhang, and H. Amakawa. 1997. "The Fractionation Between Y and ho in the Marine Environment." *Earth and Planetary Science Letters* 148: 329–340. https://doi.org/10.1016/S0012-821X(97)00034-4.

Och, L. M., and G. A. Shields-Zhou. 2012. "The Neoproterozoic Oxygenation Event: Environmental Perturbations and Biogeochemical Cycling." *Earth-Science Reviews* 110: 26–57. https://doi.org/10.1016/j.earscirev.2011.09.004.

Olivarez, A. M., and R. M. Owen. 1991. "The Europium Anomaly of Seawater: Implications for Fluvial versus Hydrothermal REE Inputs to the Oceans." *Chemical Geology* 92: 317–328. https://doi.org/10.1016/0009-2541(91)90076-4.

O'Nions, R. K., S. R. Carter, R. S. Cohen, N. M. Evensen, and P. J. Hamilton. 1978. "Pb, Nd and Sr Isotopes in Oceanic Ferromanganese Deposits and Ocean Floor Basalts." *Nature* 273: 435–438. https://doi.org/10.1038/273435a0.

Ootes, L., W. J. Davis, V. A. Jackson, and O. van Breemen. 2015. "Chronostratigraphy of the Hottah Terrane and Great Bear Magmatic Zone of Wopmay Orogen, Canada, and Exploration of a Terrane Translation Model." *Canadian Journal of Earth Sciences* 52: 1062–1092. https://doi.org/10.1139/cjes-2015-0026.

Ootes, L., V. A. Jackson, W. J. Davis, V. Bennett, L. Smar, and B. L. Cousens. 2016. "Parentage of Archean Basement Within a Paleoproterozoic Orogen and Implications for on-Craton Diamond Preservation: Slave Craton and Wopmay Orogen, Northwest Canada1." *Canadian Journal of Earth Sciences* 54: 203–232. https://doi.org/10.1139/cjes-2016-0059.

Pesonen, L. J., D. A. D. Evans, T. Veikkolainen, J. Salminen, and S.-Å. Elming. 2021. "Chapter 1–Precambrian Supercontinents and Supercycles—An Overview." In *Ancient Supercontinents and the Paleogeography of Earth*, edited by L. J. Pesonen, J. Salminen, S.-Å. Elming, D. A. D. Evans, and T. Veikkolainen, 1–50. Amsterdam: Elsevier. https://doi.org/10.1016/B978-0-12-818533-9.00020-5.

Piepgras, D. J., and G. J. Wasserburg. 1985. "Strontium and Neodymium Isotopes in Hot Springs on the East Pacific Rise and Guaymas Basin." *Earth and Planetary Science Letters* 72: 341–356. https://doi.org/10.1016/0012-821X(85)90057-3.

Planavsky, N., A. Bekker, O. J. Rouxel, et al. 2010. "Rare Earth Element and Yttrium Compositions of Archean and Paleoproterozoic Fe Formations Revisited: New Perspectives on the Significance and Mechanisms of Deposition." *Geochimica et Cosmochimica Acta* 74: 6387–6405. https://doi.org/10.1016/j.gca.2010.07.021.

Planavsky, N., O. Rouxel, A. Bekker, R. Shapiro, P. Fralick, and A. Knudsen. 2009. "Iron-Oxidizing Microbial Ecosystems Thrived in Late Paleoproterozoic Redox-Stratified Oceans." *Earth and Planetary Science Letters* 286: 230–242. https://doi.org/10.1016/j.epsl.2009.06.033.

Planavsky, N. J., D. Asael, A. Hofmann, et al. 2014. "Evidence for Oxygenic Photosynthesis Half a Billion Years Before the Great Oxidation Event." *Nature Geoscience* 7: 283–286. https://doi.org/10.1038/ngeo2122.

Poitrasson, F. 2006. "On the Iron Isotope Homogeneity Level of the Continental Crust." *Chemical Geology* 235: 195–200. https://doi.org/10.1016/j.chemgeo.2006.06.010.

Pope, M. C., and J. P. Grotzinger. 2003. "Paleoproterozoic Stark Formation, Athapuscow Basin, Northwest Canada: Record of Cratonic-Scale Salinity Crisis." *Journal of Sedimentary Research* 73: 280–295. https://doi.org/10.1306/091302730280.

Pourmand, A., N. Dauphas, and T. J. Ireland. 2012. "A Novel Extraction Chromatography and MC-ICP-MS Technique for Rapid Analysis of REE, Sc and Y: Revising CI-Chondrite and Post-Archean Australian Shale (PAAS) Abundances." *Chemical Geology* 291: 38–54. https://doi.org/10.1016/j.chemgeo.2011.08.011.

Rantamäki, S., J. Meriluoto, L. Spoof, E.-M. Puputti, T. Tyystjärvi, and E. Tyystjärvi. 2016. "Oxygen Produced by cyanobacteria in Simulated Archaean Conditions Partly Oxidizes Ferrous Iron but Mostly Escapes—Conclusions About Early Evolution." *Photosynthesis Research* 130: 103–111. https://doi.org/10.1007/s11120-016-0231-4.

Rasmussen, B., I. R. Fletcher, A. Bekker, J. R. Muhling, C. J. Gregory, and A. M. Thorne. 2012. "Deposition of 1.88-Billion-Year-Old Iron Formations as a Consequence of Rapid Crustal Growth." *Nature* 484: 498–501. https://doi.org/10.1038/nature11021.

Roscoe, S. M., S. S. Gandhi, B. W. Charbonneau, Y. T. Maurice, and R. A. Gibb. 1987. "Mineral Resource Assessment of the Area in the East Arm (Great Slave Lake) and Artillery Lake region, N.W.T., Proposed as a National Park (NTS 75 J, K, L, N, O). Geological Survey of Canada, Open File 1434. 92p." https://doi.org/10.4095/130215.

Rounds, S. 2011. "Analysis to Support the Replacement of Weiss (1970) Equations by Benson and Krause (1980, 1984) Equations for USGS Computation of Solubility of Dissolved Oxygen in Water." U.S. Geological Survey, Office of Water Quality Technical Memorandum 2011.03, Portland, Oregon.

Rouxel, O., W. Shanksiii, W. Bach, and K. Edwards. 2008. "Integrated Fe- and S-Isotope Study of Seafloor Hydrothermal Vents at East Pacific Rise 9–10 N." *Chemical Geology* 252: 214–227. https://doi.org/10.1016/j.chemgeo.2008.03.009.

Rye, R., and H. D. Holland. 1998. "Paleosols and the Evolution of Atmospheric Oxygen: A Critical Review." *American Journal of Science* 298: 621–672. https://doi.org/10.2475/ajs.298.8.621.

Sander, R. 2023. "Compilation of Henry's Law Constants (Version 5.0.0) for Water as Solvent." *Atmospheric Chemistry and Physics* 23: 10901–12440. https://doi.org/10.5194/acp-23-10901-2023.

Schneider, D. A., M. E. Bickford, W. F. Cannon, K. J. Schulz, and M. A. Hamilton. 2002. "Age of Volcanic Rocks and Syndepositional Iron Formations, Marquette Range Supergroup: Implications for the Tectonic Setting of Paleoproterozoic Iron Formations of the Lake Superior Region." *Canadian Journal of Earth Sciences* 39: 999–1012. https://doi.org/10.1139/e02-016.

Severmann, S., T. W. Lyons, A. Anbar, J. McManus, and G. Gordon. 2008. "Modern Iron Isotope Perspective on the Benthic Iron Shuttle and the Redox Evolution of Ancient Oceans." *Geology* 36: 487. https://doi.org/10.1130/G24670A.1.

Severmann, S., J. McManus, W. M. Berelson, and D. E. Hammond. 2010. "The Continental Shelf Benthic Iron Flux and Its Isotope Composition." *Geochimica et Cosmochimica Acta* 74: 3984–4004. https://doi.org/10.1016/j.gca.2010.04.022.

Sheen, A. I., L. M. Heaman, B. Kjarsgaard, L. Ootes, D. G. Pearson, and R. A. Creaser. 2019. "Athapuscow Aulacogen Revisited: Geochronology and Geochemistry of the 2046 ma Union Island Group Mafic Magmatism, East Arm of Great Slave Lake, Northwest Territories, Canada." *Precambrian Research* 321: 85–102. https://doi.org/10.1016/j.precamres.2018.11.012.

Sholkovitz, E. R., and H. Elderfield. 1988. "Cycling of Dissolved Rare Earth Elements in Chesapeake Bay." *Global Biogeochemical Cycles* 2: 157–176. https://doi.org/10.1029/GB002i002p00157.

Sholkovitz, E. R., T. J. Shaw, and D. L. Schneider. 1992. "The Geochemistry of Rare Earth Elements in the Seasonally Anoxic Water Column and Porewaters of Chesapeake Bay." *Geochimica et Cosmochimica Acta* 56: 3389–3402. https://doi.org/10.1016/0016-7037(92)90386-W.

Sindol, G. P., M. G. Babechuk, J. Conliffe, J. F. Slack, C. Rosca, and R. Schoenberg. 2022. "Shallow-Ocean and Atmospheric Redox Signatures Preserved in the ca. 1.88 Ga Sokoman Iron Formation, Labrador Trough, Canada." *Precambrian Research* 379: 106750. https://doi.org/10.1016/j.precamres.2022.106750.

Smith, A. J. B., N. J. Beukes, J. Gutzmer, A. D. Czaja, C. M. Johnson, and N. Nhleko. 2017. "Oncoidal Granular Iron Formation in the Mesoarchaean Pongola Supergroup, Southern Africa: Textural and Geochemical Evidence for Biological Activity During Iron Deposition." *Geobiology* 15: 731–749. https://doi.org/10.1111/gbi.12248.

Steadman, J. A., R. R. Large, N. J. Blamey, et al. 2020. "Evidence for Elevated and Variable Atmospheric Oxygen in the Precambrian." *Precambrian Research* 343: 105722. https://doi.org/10.1016/j.precamres.2020.105722.

Sverjensky, D. A. 1984. "Europium Redox Equilibria in Aqueous Solution." *Earth and Planetary Science Letters* 67: 70–78. https://doi.org/10.1016/0012-821X(84)90039-6.

Swanner, E. D., A. M. Mloszewska, O. A. Cirpka, R. Schoenberg, K. O. Konhauser, and A. Kappler. 2015. "Modulation of Oxygen Production in Archaean Oceans by Episodes of Fe(II) Toxicity." *Nature Geoscience* 8: 126–130. https://doi.org/10.1038/ngeo2327.

Swanner, E. D., W. Wu, R. Schoenberg, et al. 2015. "Fractionation of Fe Isotopes During Fe(II) Oxidation by a Marine Photoferrotroph Is Controlled by the Formation of Organic Fe-Complexes and Colloidal Fe Fractions." *Geochimica et Cosmochimica Acta* 165: 44–61. https://doi.org/10.1016/j.gca.2015.05.024.

Tanaka, T., S. Togashi, H. Kamioka, et al. 2000. "JNdi-1: A Neodymium Isotopic Reference in Consistency With LaJolla Neodymium." *Chemical Geology* 168: 279–281. https://doi.org/10.1016/S0009-2541(00)00198-4.

Tebo, B. M., H. A. Johnson, J. K. McCarthy, and A. S. Templeton. 2005. "Geomicrobiology of Manganese(II) Oxidation." *Trends in Microbiology* 13: 421–428. https://doi.org/10.1016/j.tim.2005.07.009.

Thompson, K. J., P. A. Kenward, K. W. Bauer, et al. 2019. "Photoferrotrophy, Deposition of Banded Iron Formations, and Methane Production in Archean Oceans." *Science Advances* 5: eaav2869. https://doi.org/10.1126/sciadv.aav2869.

Toma, J., C. Holmden, P. Shakotko, Y. Pan, and L. Ootes. 2019. "Cr Isotopic Insights Into ca. 1.9 Ga Oxidative Weathering of the Continents

Using the Beaverlodge Lake Paleosol, Northwest Territories." *Canada. Geobiology* 17: 467–489. https://doi.org/10.1111/gbi.12342.

Trouwborst, R. E., A. Johnston, G. Koch, G. W. Luther, and B. K. Pierson. 2007. "Biogeochemistry of Fe(II) Oxidation in a Photosynthetic Microbial Mat: Implications for Precambrian Fe(II) Oxidation." *Geochimica et Cosmochimica Acta* 71: 4629–4643. https://doi.org/10.1016/j.gca.2007.07.018.

Trower, E. J., M. P. Lamb, and W. W. Fischer. 2017. "Experimental Evidence That Ooid Size Reflects a Dynamic Equilibrium Between Rapid Precipitation and Abrasion Rates." *Earth and Planetary Science Letters* 468: 112–118. https://doi.org/10.1016/j.epsl.2017.04.004.

Tsikos, H., A. Matthews, Y. Erel, and J. M. Moore. 2010. "Iron Isotopes Constrain Biogeochemical Redox Cycling of Iron and Manganese in a Palaeoproterozoic Stratified Basin." *Earth and Planetary Science Letters* 298: 125–134. https://doi.org/10.1016/j.epsl.2010.07.032.

Van Breemen, O., B. A. Kjarsgaard, S. Tella, D. Lemkow, and L. Aspler. 2013. "U-Pb Detrital Zircon Geochronology of Clastic Sedimentary Rocks of the Paleoproterozoic Nonacho and East Arm Basins." Thaidene Nene MERA Study Area (No. 7196) https://doi.org/10.4095/292453.

van de Flierdt, T., A. M. Griffiths, M. Lambelet, S. H. Little, T. Stichel, and D. J. Wilson. 2016. "Neodymium in the Oceans: A Global Database, a Regional Comparison and Implications for Palaeoceanographic Research." *Philosophical Transactions. Series A, Mathematical, Physical, and Engineering Sciences* 374: 20150293. https://doi.org/10.1098/rsta.2015.0293.

Walter, M. R., A. D. T. Goode, and W. D. M. Hall. 1976. "Microfossils From a Newly Discovered Precambrian Stromatolitic Iron Formation in Western Australia." *Nature* 261: 221–223. https://doi.org/10.1038/261221a0.

Wang, C., M. A. Lechte, C. T. Reinhard, et al. 2022. "Strong Evidence for a Weakly Oxygenated Ocean–Atmosphere System During the Proterozoic." *Proceedings of the National Academy of Sciences* 119: e2116101119. https://doi.org/10.1073/pnas.2116101119.

Wang, C., L. J. Robbins, N. J. Planavsky, et al. 2023. "Archean to Early Paleoproterozoic Iron Formations Document a Transition in Iron Oxidation Mechanisms." *Geochimica et Cosmochimica Acta* 343: 286–303. https://doi.org/10.1016/j.gca.2022.12.002.

Wang, C., M. Zhai, L. J. Robbins, Z. Peng, X. Zhang, and L. Zhang. 2024. "Late Archean Shelf-to-Basin Iron Shuttle Contributes to the Formation of the World-Class Dataigou Banded Iron Formation." *Economic Geology* 119: 725–736. https://doi.org/10.5382/econgeo.5047.

Weber, B., E. E. Scherer, U. K. Martens, and K. Mezger. 2012. "Where Did the Lower Paleozoic Rocks of Yucatan Come From? A U–Pb, Lu–Hf, and Sm–Nd Isotope Study." *Chemical Geology* 312-313: 1–17. https://doi.org/10.1016/j.chemgeo.2012.04.010.

Zhang, S., X. Wang, H. Wang, et al. 2016. "Sufficient Oxygen for Animal Respiration 1,400 Million Years Ago." *Proceedings of the National Academy of Sciences* 113: 1731–1736. https://doi.org/10.1073/pnas.1523449113.

Supporting Information

Additional supporting information can be found online in the Supporting Information section.